Materials & Design 258 (2025) 114592

Contents lists available at ScienceDirect

Materials & Design

journal homepage: www.elsevier.com/locate/matdes

Effect of heat treatment on the recrystallisation of thin-walled stainless steel 316L fabricated by laser beam powder bed fusion☆

Charlie Bevan [a], Nicholas Barnard [a], Thomas Jones [b], Robert Lancaster [a,*]

[a] Institute of Structural Materials, Swansea University, Bay Campus, Swansea, SA1 8EN, United Kingdom
[b] Rolls-Royce plc., Kings Place, 90 York Way, London N1 9FX United Kingdom

ARTICLE INFO

Keywords:
Laser beam powder bed fusion (LB-BPF)
Stainless steel 316L (SS316L)
Post-processing
Heat-treatment (HT)
Recrystallisation

ABSTRACT

Additive Manufacturing (AM), particularly laser beam powder bed fusion (LB-PBF), enables fabrication of complex thin-wall geometries, yet post-processing studies on such structures are limited. This work investigates heat-treatment annealing of thin-walled stainless steel 316L (SS316L) built via LB-PBF. A novel build geometry with wall thicknesses from 0.2–1.8 mm was used to examine microstructures before and after heat-treatment (HT) at 1050 °C and 1150 °C. In the as-built state, thinner walls showed grains oriented in <001> toward the wall centre, while thicker walls exhibited a <101> orientation due to a central band of preferential grain growth, typical of larger LB-PBF SS316L parts. Annealing at 1150 °C produced partial recrystallisation in all samples, reaching 86 % in the thickest walls, whereas 1050 °C annealing had little effect. Analysis of geometrically necessary dislocation density, low-angle boundaries (LAB), and high-angle boundaries (HAB) showed no correlation with recrystallisation behaviour. The primary factor limiting recrystallisation was Mn- and Si-based oxide distributions, which impeded grain boundary migration. This caused a stop-and-go growth mechanism, leading to abnormal grain growth in some cases. Findings highlight that chemical segregation, rather than dislocation structure, controls recrystallisation in thin-walled LB-PBF SS316L.

1. Introduction

Laser powder bed fusion (LB-PBF) is one of the leading additive manufacturing technologies that allows the fabrication of highly complex and thin-walled geometries that are usually not viable through other, more conventional manufacturing means. Thin-walled geometries are typically used in heat exchanger applications, where the fast exchange of heat is solely affected by the constraints of part geometry [1]. With the constant evolution of the AM industry and the continual development of LB-PBF based processes, the constraints of such manufacturing methods must be understood and are of great importance to fully realise the potential of the technologies.

LB-PBF technologies mostly utilise a laser beam system that interacts and sinters metallic powder particles. The components are then created through a layer-by-layer process; the component is split up unto 2-D layers and the step-by step process is repeated until a 3-D component of the desired geometry has been created [2]. During the process, interactions between the laser beam and powder create melt pools [3]. Once a successive pass over an already sintered layer is complete, the next pass will penetrate and remelt numerous layers below and give rise to the unique and intricate fish-scale microstructure [4]. The size and distribution of such features is dictated by the underlying process parameters, which need careful manipulation in order to produce a fully optimised process and near fully dense final component [5].

An alloy that is used in many industrial applications is stainless steel 316L (SS316L). SS316L has been extensively studied due to its excellent processability, corrosion resistance, and mechanical properties, making it popular in aerospace and submarine sectors [1,6]. The as-built microstructure of LB-PBF SS316L consists of fine solidification cells of face-centered cubic (FCC) austenite [7]. The microstructure is typically anisotropic in nature [8], which is a result of the complex localised cyclic heating and cooling regime [3,9,10]. As such, epitaxial grain growth is dominant where subsequent grains span across multiple melt pools, aligned parallel to the build direction. Much research has discussed the heterogeneity of the microstructure of larger LB-PBF SS316L components, including laboratory test coupons [11–16], but reported research on thin walled components below 1 mm in thickness is notably sparse. Since the thermal history within these samples will vary

☆ This article is part of a special issue entitled: 'Additive Manufacturing' published in Materials & Design.

* Corresponding author.
E-mail address: r.j.lancaster@swansea.ac.uk (R. Lancaster).

https://doi.org/10.1016/j.matdes.2025.114592
Received 11 March 2025; Received in revised form 13 August 2025; Accepted 13 August 2025
Available online 14 August 2025

significantly from that of bulkier components, there is a clear necessity for understanding such behaviours given the breadth of industrial sectors and components that look to adopt thinner walled structures in their designs. Wrobel et al. [17] reported that thinner single and double track samples featured finer grains with a more pronounced <100> texture, whereas thicker samples displayed larger grains oriented parallel to the build direction, with a pronounced <101> texture. This difference was attributed to the underlying melt pool size and microstructure which varied with wall thickness, which in turn influenced both the grain size and orientation. The single track samples exhibited symmetric elliptical melt pools as a result of uniform denudation. This symmetry was also observed in the initial tracks across other thicknesses. However, in thicker walls, melt pools located toward the centre tended to be deeper and less symmetrical, leading to an uneven, undulating upper surface.

Microstructural anisotropy in LB-PBF components can be detrimental to the mechanical performance due to the directional dependence, which can lead to inconsistencies in the properties and prove problematic in parts subjected to multiaxial stress fields [8]. Such features can manifest as reduced strength, ductility, and fatigue resistance in certain directions, compromising the overall integrity and functionality of the component. Annealing heat treatment (HT) processes [18] are commonly used to alleviate this susceptibility and suppress associated anisotropy through promoting recrystallisation and homogenisation of the microstructure [19]. This process also aids in reducing built-up residual stress and produces a more uniform grain morphology [20,21], thereby enhancing the homogeneity of the material and improving the mechanical properties and reliability of LB-PBF components.

During annealing, recrystallisation can be influenced by several factors, including initial grain size, stored dislocation energy, and the presence of oxide particles [22–24]. Oxide particles, which may originate from the powder feedstock or form during processing, through elements reacting with residual oxygen [23], can act as pinning agents that hinder grain boundary motion, delaying or suppressing recrystallisation. This particle pinning effect plays a critical role in controlling grain growth and overall microstructural evolution [25]. Understanding these factors is essential for optimising HT parameters to achieve desired mechanical properties in LB-PBF produced thin-walled components. Many researchers have investigated the recrystallisation kinetics from heat-treating larger LB-PBF SS316L geometries to alleviate anisotropy and texture effects [26–29]. Furthermore, researchers [23–25,30] also investigated annealing of LB-PBF 316L stainless steel and found oxide pinning to be the main mechanism in delayed recrystallisation behaviour. However, no reported literature is available that discusses related behaviours on thin-walled structures, where factors such as heat dissipation, oxide precipitation, and geometric scale can significantly influence recrystallisation kinetics.

In this study, the effect of HT on the microstructures of thin-walled LB-PBF SS316L structures is investigated. The grain morphology and texture of each individual wall from 0.2 mm up to 1.8 mm has been analysed through EBSD, for both as-built and alternative heat-treated states. Further analysis is presented that elaborates on the effect of geometrically necessary dislocation density (GNDs) on recrystallisation, in addition to presence, and subsequent effect of oxides particle pinning.

2. Materials and experimental methods

2.1. Materials & samples

In this study, a series of four novel build geometries were manufactured from virgin SS316L powder using laser powder bed fusion (LB-PBF). The ladder geometries were specifically designed to explore the influence of heat treatments and the associated recrystallisation behaviour in thin-walled structures of varying thicknesses. The ladder components consisted of a series of varying wall thicknesses ranging from 0.2 mm to 2 mm, as depicted schematically in Fig. 1. The figure is a cut through visual of the ladder geometry from the XZ microstructural plane.

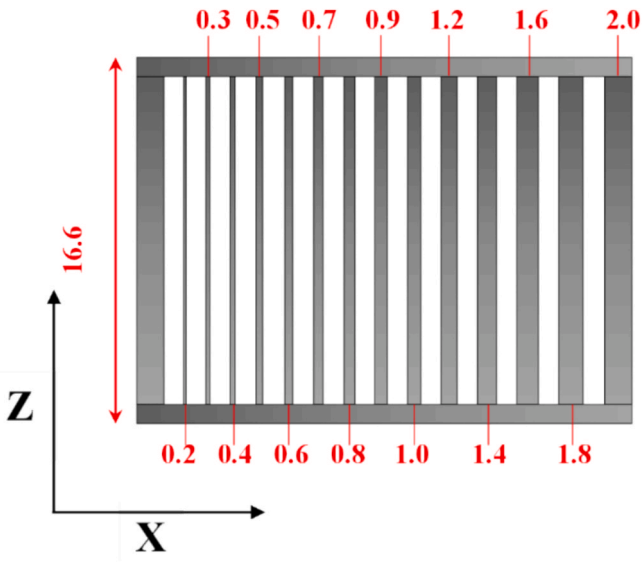

Fig. 1. Schematic diagram of the XZ microstructural plane of the LB-PBF SS316L ladder geometry with varying wall thicknesses.

The ladder component described was built on an EOS M290 LB-PBF machine, with a powder size distribution ranging from 10-49 μm, each of which were built with an equivalent energy density of 100 J/mm^3 and a layer thickness of 20 μm. The composition and particle size distribution of the virgin SS316L powder is given in Tables 1 and 2. The scanning patterns for the thinnest (0.2 mm) and thickest walls (1.8 mm) are represented in Fig. 2. In each scan pattern, the laser direction is rotated after every layer by 67°, which is illustrated by arrows in Fig. 2.

2.2. Post-processing procedures

Post manufacture, the ladder geometries were subjected to one of three alternative heat treatments. The specific parameters for the heat treatments are provided within Table 3. The fourth ladder sample remained in the as-built condition with no additional post-processing to provide a baseline entity of the material prior to heat-treatment. All the post-process heat treatments were completed at ambient pressure within a programmable box furnace utilising consistent heating and cooling rates of <10 °C/s. The temperature control tolerance was set at +/- 5 °C and measured using a Pico Logger accompanied with the Pico Logger 6 software. A hold time of 135 min was chosen to remain consistent with previous studies by the authors [31,32].

After HT, the samples were sectioned relatively close to the inner wall, parallel to the build direction on a Struers Brilliant – 200 appliance. The XZ microstructural plane (parallel to the build direction) was chosen for characterisation to avoid misleading recrystallisation calculations that might occur when investigating the XY plane (perpendicular to the build direction).

2.3. Microstructural characterisation

Prior to microscopic analysis, the samples were prepared using standard metallographic techniques, starting with initial grinding and successively finer grit cloths, concluding with an MD-Chem polishing cloth with a 0.04 μm OP-S suspension to achieve a reflective, mirror-like finish. The microstructure and oxide particles were analysed using a Hitachi SU-3500 scanning electron microscope (SEM). The oxide chemistries were analysed using energy dispersive X-ray spectroscopy (EDS), with the help of backscattered imaging. The texture and grain orientation were measured using electron-backscattered diffraction

Table 1
Composition of stainless steel 316L powder.

Element	C	Cr	Ni	Mo	Si	Fe	Mn	S	P	N	O (ppm)
(%)	0.01	16.87	12.41	2.32	0.57	base	1.2	0.002	0.008	0.11	341

Table 2
Particle size distribution of stainless steel 316L powder.

D_x Number	D_1	D_{25}	D_{50}	D_{75}	D_{90}
Particle Size Diameter (μm)	10–16	20–26	26–32	34–40	43–49

(EBSD). The main operating parameters selected for both techniques were 20 kV accelerating voltage and a spot size of 90. The EBSD required a step size and exposure time of 0.59 μm and 10 μs, respectively. In the interpretation of the EBSD maps, low angle boundaries (LAB) were defined as having a local misorientation <15° and high angle boundaries (HAB) defined as >15° misorientation. Texture analysis followed a threshold value whereby samples exhibiting maximum multiples of unity distribution (MUD) values >3, could therefore be classed as 'textured'. Grain size and aspect ratio measurements for all microstructures were determined using the mean linear intercept method.

Additional imaging was collected on a JEOL 7800F field emission gun (FEG) SEM equipped with a tungsten source. For particle analysis, a backscattered electron (BSE) image was captured at an accelerating voltage of 20 keV with a medium probe current of 9, corresponding to the electron beam's spot size.

Grain orientation spread (GOS) is a critical metric used to assess the degree of plastic deformation within grains, which can serve as an indicator for recrystallisation during post- processing. GOS quantifies the misorientation within individual grains by measuring the angular difference between neighbouring points inside a grain, as identified using the in-built algorithm in the Channel5 software. Low GOS values generally suggest fully recrystallised grains, while higher GOS values are indicative of deformed or partially recrystallised grains. In this study, GOS was employed to calculate the extent of recrystallisation in the LB-PBF SS316L samples. EBSD maps were generated for each sample, and grain-level misorientations were computed to derive GOS values, through the software. Grains with GOS values below a certain threshold, typically less than 2°, were classified as recrystallised. This threshold is based on prior studies [13,28,33] that have demonstrated a correlation between low GOS and fully recrystallised grains. The final area percentage was calculated by summing the areas of all grains with a GOS value below the 2° threshold.

2.4. Mechanical testing

Vickers microhardness testing was used to obtain relative mechanical data for all wall thicknesses from each of the four HT conditions. Hardness testing was completed on a Struers Duramin-A40, to investigate correlations between localised mechanical properties and microstructure. A 50 g force with a 10 s dwell time was used, to prevent the smaller walls with much less material volume from over-deforming or rupturing under a higher load. Additionally, using 50 g ensured that the deformation during testing was not influenced by the outer-wall regions and permitted representative sampling. A testing pattern consisting of 1 row with 10 individual points was applied to directly test the central regions of each wall.

3. Results

3.1. Microstructural behaviour

3.1.1. As-built

Examination of the as-built material revealed the microstructure

Table 3
Post manufacture heat-treatment parameters for LB-PBF SS316L ladder geometries.

Heat Treatment No.	Temperature (°C)	Hold Time (Minutes)	Heating/Cooling Rate (°C/Min)
HT1	1050	135	<10
HT2	1150	135	<10
HT3	1200	135	<10

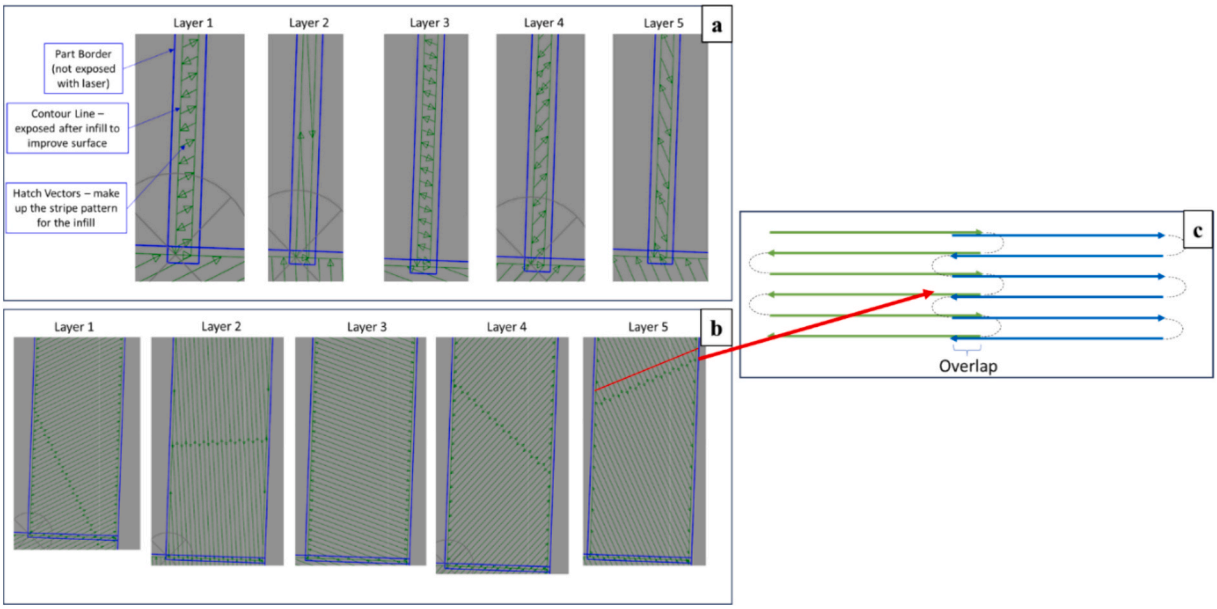

Fig. 2. Scanning pattern for LB-PBF SS316L ladder geometries: a) 0.2 mm wall thickness, b) 1.8 mm wall thickness, and c) representation of overlap region.

exhibited behaviour typically observed in AM, mirroring the findings reported in previous literature [12,14,34]. As shown in Fig. 3, the microstructure of all as-built samples is dominated by a columnar grain structure, reflecting epitaxial grain growth across multiple melt pool boundaries and span through multiple build layers. This occurs irrespective of the change in wall thickness. However, a variation in grain size and orientation is evident across the different samples, as presented in Table 4. The most obvious differences were observed in the three thinnest samples (Fig. 3(a–c)) compared to the thicker walls exceeding 0.4 mm. In the former, grain growth tended towards the central regions of the wall and converge at the end of each grain. This grain alignment corresponds to the semi-elliptical and symmetrical formation of the melt pool investigated and discussed by Wrobel et al. [17]. Consequently, the main driver for solidification is the thermal gradient (G), oriented perpendicular to the melt pool boundaries and extending toward the top central region. Therefore, the grain morphology seemingly orients towards the wall centre with crystallographic texture more defined toward the <001>, represented through the inverse pole figures, as shown in Fig. 4.

However, due to the relative sample size, the maximum MUD values were less than 3, indicating that even though some crystallographic texture is evident, it is not thought to be high enough to be considered a heavily textured microstructure. Likewise, this value is likely skewed by the presence of refined equiaxed grains at the edges of the walls. An increased wall thickness exhibited a general increase in grain size and the maximum MUD value, indicating that larger grains with a stronger crystallographic texture become more prominent. This coincides with a reduction in the relative frequency of low angle grain boundaries.

As the wall thickness is increased to 0.5 mm (Fig. 3d)), the grains present maintained some alignment towards the central region but are predominantly aligned parallel to the build direction. These microstructures closely resemble those depicted previously by Wrobel et al. [17]. Furthermore, the aspect ratio remains relatively stable (0.19–0.23) across all thicknesses, indicating that even though the alignment changes, grains are not significantly elongating or compressing with changes in thickness.

It is evident from Fig. 4 that the observed grain morphology changes and this consequently influences the texture of each sample. As shown, for the thinner samples (Fig. 4a)–c)) the MUD value tends toward the <001>, however these values are below the threshold for the material to be considered textured. The limiting factor in this scenario is sample size, as all calculations are relative to each sample. Due to this, MUD values may be lower than visually presented. With an increase in sample thickness, the more prominent <101> starts to evolve throughout the samples, which is particularly evident in the 1.8 mm thick sample. Furthermore, this sample has two clear bands of grain orientation, where approximately 500 μm from the wall edge, grains are seen growing at a 45° angle towards the central band of material.

In regard to the thicker samples, Fig. 3d)–h), the solidification microstructure results from the increased cooling rates due to slower heat dispersion. As a result, solidification behaves in a manner similar to that of bulkier samples, whereby a more pronounced <101> texture is prominent, akin to that reported in the literature [7,27,35–37]. This is a known grain orientation that LB-PBF SS316L microstructures tends toward.

It has been established that the thermal gradient is different in samples with varying wall thickness. In Fig. 3d), there is the first distinguished change in grain morphology which involves a central band of <101> textured grains running parallel to the build direction, bordered by smaller, randomly oriented grains growing at a 45° angle from the wall edges. Due to heat dissipation, the larger central band retains heat across successive powder layers, allowing the grains to continuously grow epitaxially in the preferred <101> orientation. In contrast, the grains near the outer edge cool much faster, leading to reduced grain growth, which is directed toward the central band, driven by the thermal gradient created by the central grains.

Another significant consideration is the scan pattern used across the different wall thicknesses. The representative scanning pattern

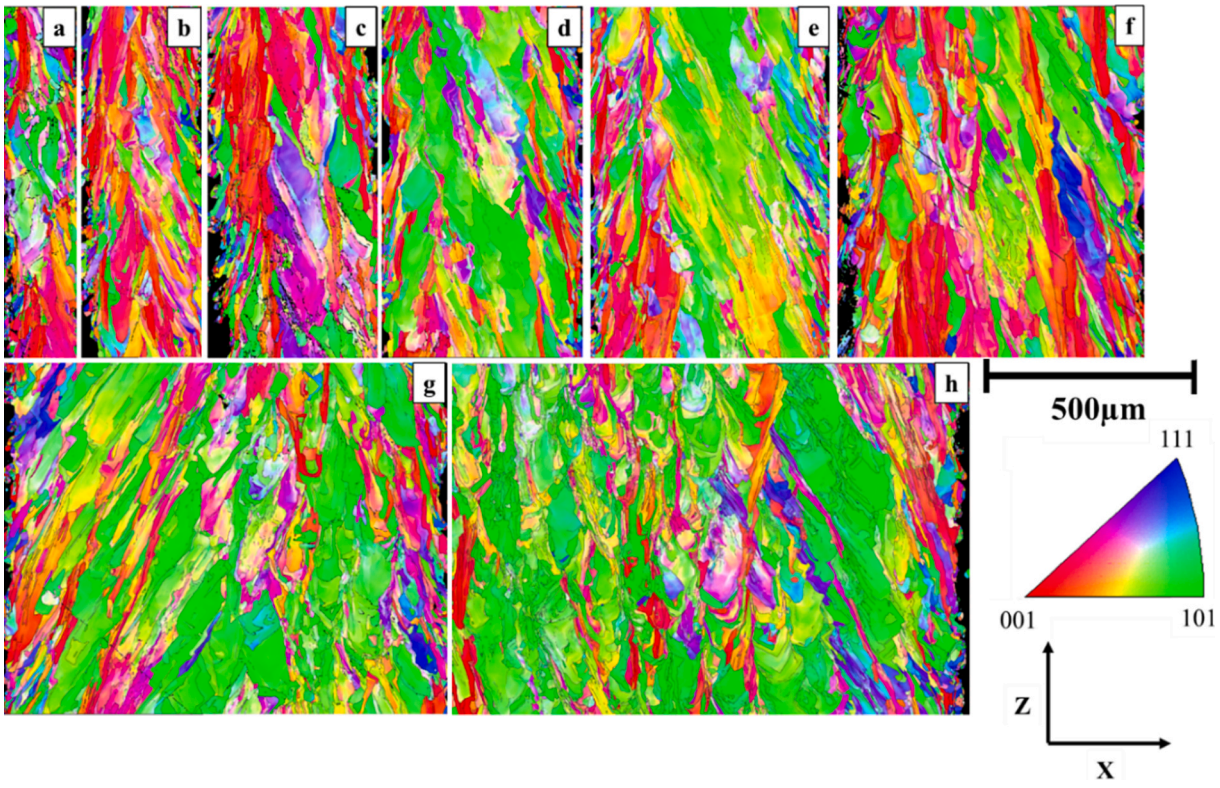

Fig. 3. Inverse pole figure maps of as-built LB-PBF SS316L thin-walled samples – XZ microstructural plane: a) 0.2 mm, b) 0.3 mm, c) 0.4 mm, d) 0.5 mm, e) 0.6 mm, f) 0.8 mm, g) 1 mm and h) 1.8 mm wall edge.

Table 4
Microstructural parameters for LB-PBF as-built SS316L thin-walled samples.

Thickness (mm)	Mean Grain size (μm^2)	Aspect ratio	LAB relative frequency	GND Density ($10^{14}/m^2$)	Twin Boundaries (Σ3) (%)	Maximum MUD
0.2	208	0.22	0.916	1.24	0.08	1.70
0.3	223	0.18	0.875	1.26	0.12	2.55
0.4	278	0.21	0.912	1.20	0.16	2.07
0.5	302	0.22	0.791	1.32	0.24	3.16
0.6	298	0.19	0.803	1.33	0.19	3.46
0.8	300	0.19	0.729	1.37	0.12	2.46
1	270	0.20	0.785	1.30	0.19	3.12
1.8	345	0.23	0.756	1.39	0.39	3.45

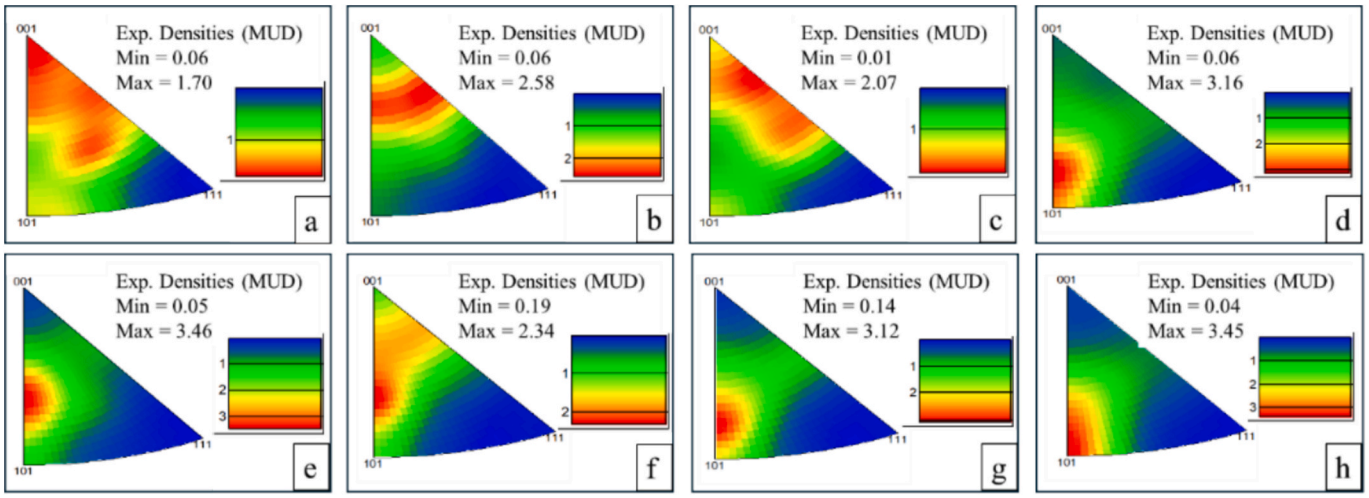

Fig. 4. Inverse pole figures of as-built LB-PBF SS316L thin-walled samples – XZ microstructural plane: a) 0.2 mm, b) 0.3 mm, c) 0.4 mm, d) 0.5 mm, e) 0.6 mm, f) 0.8 mm, g) 1 mm and f) 1.8 mm wall edge.

regarding the thinner as-built walls (0.2–0.4 mm), induces apparent differences in heating effects on the build layers. At these lower thicknesses, having very small material volume per build layer, accompanied with the time it takes to sinter the succeeding layer, the material has already cooled to a point where, when the next layer is deposited there will be a relatively large thermal gradient between the layers, as reported previously through simulation by Wrobel et al. [17].

Fig. 5 presents the geometric necessary dislocation (GND) behaviour in the as-built samples, showing similar spatial distribution and density of GNDs across varying wall thicknesses. Fig. 6 further quantifies this, indicating that while thinner samples exhibit a higher relative frequency peak of GNDs, the data is normalised per sample. Thicker samples have higher observed GND densities, as confirmed in Table 3. This suggests that thicker samples (0.5–1.8 mm) contain more stored energy for recrystallisation, as evidenced by the broader curves observed for these samples.

3.1.2. *Heat treatment 1 (1050 °C, 135 min)*

The microstructures of the LB-PBF SS316L samples subjected to Heat Treatment 1 (HT1: 1050 °C, 135 min) are presented in Fig. 7. As shown, the microstructure appears to exhibit a similar morphology to the as-built samples, with the clear presence of columnar grains aligning parallel to the build direction. These findings indicate that a temperature of 1050 °C has minimal influence on recrystallisation of LB-PBF SS316L. As a result, the first 5 walls were investigated (0.2–0.6 mm) with one further EBSD map completed at 1.8 mm to support and confirm that no recrystallisation occurred at higher wall thicknesses.

Despite HT1 appearing to have minimal effect on recrystallisation, some notable differences were observed in the HT1 samples regarding grain characteristics compared to the as-built state. For example, a reduction in the number of smaller columnar grains nucleating from the outer walls was observed. In the as-built state, it was seen that near to the outer edges of walls, nucleation of smaller grains was more prominent within thicker samples. Whereas, in HT1, the thermal input has reduced the proportion of smaller nucleating grains, as particularly evident in the thinner samples, as seen in Fig. 7a)–d). Although significant microstructural alterations were not observed, a noticeable variation emerged in relation to the reduction in sample thickness, likely due to the oxidation of the metallic samples within the post-processing procedure.

Some minor variations were also observed in terms of grain size. The HT1 samples exhibited a slightly courser columnar grain structure compared to those in the as-built condition, as supported by the data in Tables 4 and 5. However, the average aspect ratios remained consistent with those of the as-built samples, confirming the similar morphology of the respective grains. Additionally, as grain growth was observed, changes in texture also took place. In the as-built state, the grain orientation was more randomly distributed, and this absence of texture persisted in the 0.5 mm and 0.6 mm HT1 samples, as shown in Fig. 8(d) and (e), respectively. However, the three thinnest samples (0.2–0.4 mm) exhibited a tendency more towards a <001> orientation, as reflected in the MUD values displayed in Table 5.

3.1.3. *Heat treatment 2 (1150 °C, 135 min)*

As the heat treatment temperature is increased to 1150 °C (HT2), the LB-PBF SS316L thin-walled samples undergo a more pronounced level of recrystallisation, as shown in Fig. 9 and Table 6. Here, the majority of the long-columnar grains have been replaced by a mix of equiaxed, uniform, and abnormally grown homogenised grains. Notably, individual grains that span the entire wall thickness are also now evident in the thinner-walled samples (0.3–0.4 mm), also there is a near-complete reduction of as-built additive grains and an increased presence of

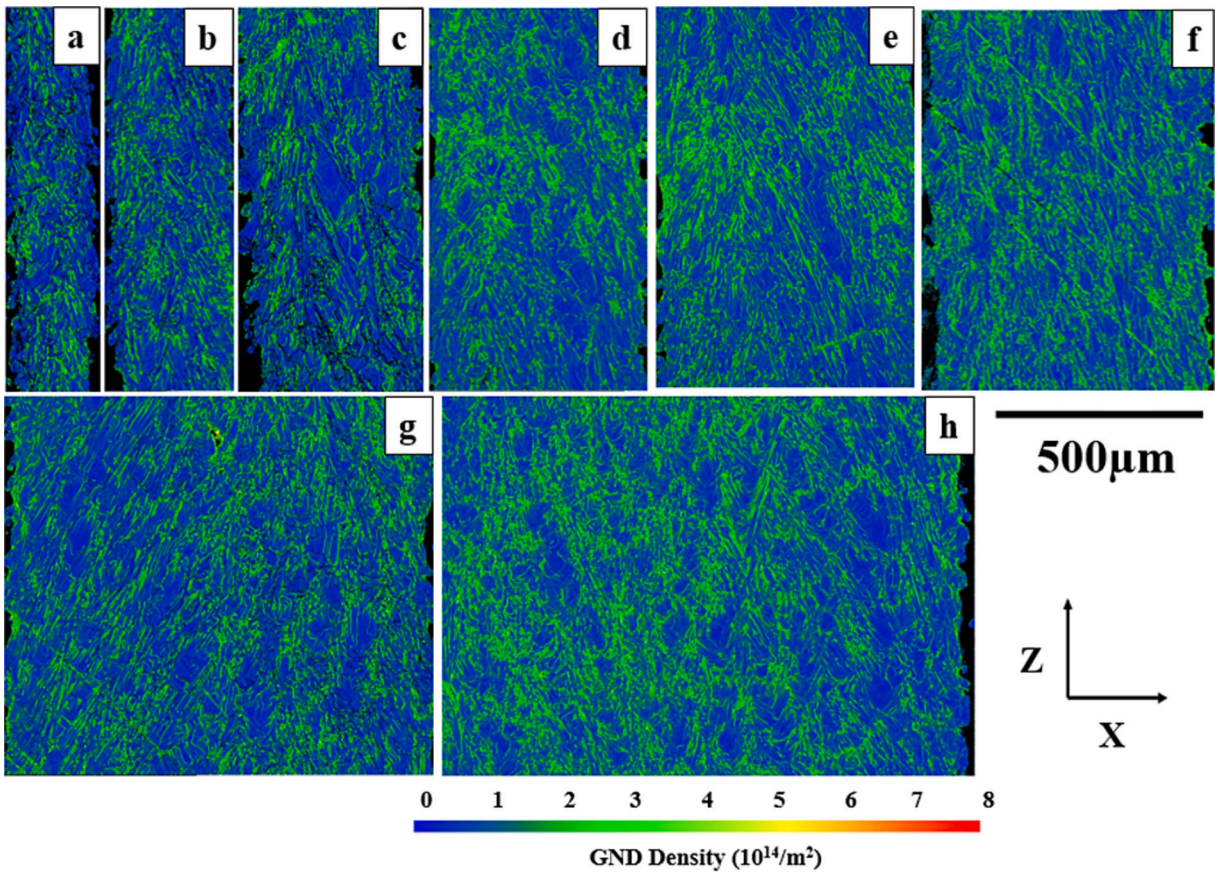

Fig. 5. Geometric necessary dislocation (GND) density maps of as-built LB-PBF SS316L thin-walled samples: a) 0.2 mm, b) 0.3 mm, c) 0.4 mm, d) 0.5 mm, e) 0.6 mm, f) 0.8 mm, g) 1 mm, h) 1.8 mm.

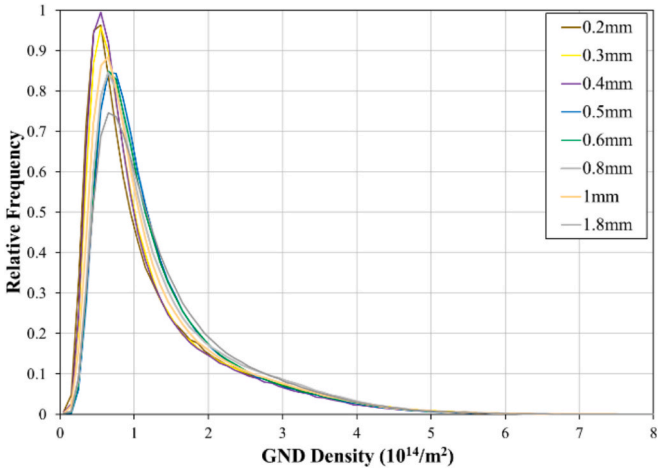

Fig. 6. GND relative frequency of as-built LB-PBF SS316L thin-walled samples.

annealing twins. With an increase in wall thickness, as-built grains are still present albeit with a preferential alignment to the <101> orientation. Despite this, the newly formed recrystallised grains can be seen to exhibit a higher degree of twinning, akin to the thinner samples discussed prior. To note, the 0.2 mm thick wall sample became fully oxidised under HT2 conditions and was unsalvageable for microscopic analysis.

As was the case for the HT1 samples, the increased temperature used in HT2 has led to a significant change in grain morphology, with an increase in grain size (by a factor of 2–3) and aspect ratio (by a factor of 1.5–2) seen across all samples. A significant increase in annealing twin boundaries was also seen, rising from below 1 % at 1050 °C, to above 20 % in some samples heat treated at 1150 °C. Although the thicker samples (0.8–1.8 mm) exhibited a larger population of grains due to the increased wall thickness, the average grain size was slightly reduced. This is due to an increase in freshly nucleated grains and competitive grain growth.

Fig. 10 illustrates the reduction in microstructural anisotropy achieved through HT2 on the LB-PBF SS316L samples, with the exception of the 0.3 mm sample. The inverse pole figure for this sample shows a strong texture with preferential alignment toward the <001> direction. The reduced material thickness, attributed to oxidation, results in a lower grain count, which can amplify the MUD value, indicating a strong crystallographic texture even with the few grains oriented to <001> . Due to a partially recrystallised microstructure, other samples show no distinct preferential orientation, with the next highest MUD value being 3.10 in Fig. 10 (c). While a MUD value above 3 indicates texture, most samples fall below or only slightly exceed this threshold, indicating minimal texture, supporting the start of isotropic recrystallisation behaviour. This is reflected by the reduced maximum MUD values, where the average MUD for HT2 samples is now 3.1, as opposed to the HT1 where the average was 3.7.

3.1.4. Heat treatment 3 (1200 °C, 135 min)

At 1200 °C (HT3), the samples exhibit near full recrystallisation across all thicknesses, resulting in a randomly oriented and predominantly equiaxed grain structure, as displayed in Fig. 11 and Table 7. The columnar grains have been replaced by a mix of equiaxed, uniform, and occasionally abnormally grown grains, with an increased presence of annealing twins compared to samples subjected to other heat treatments presented here. As the thickness is increased from 0.8 mm to 1.8 mm,

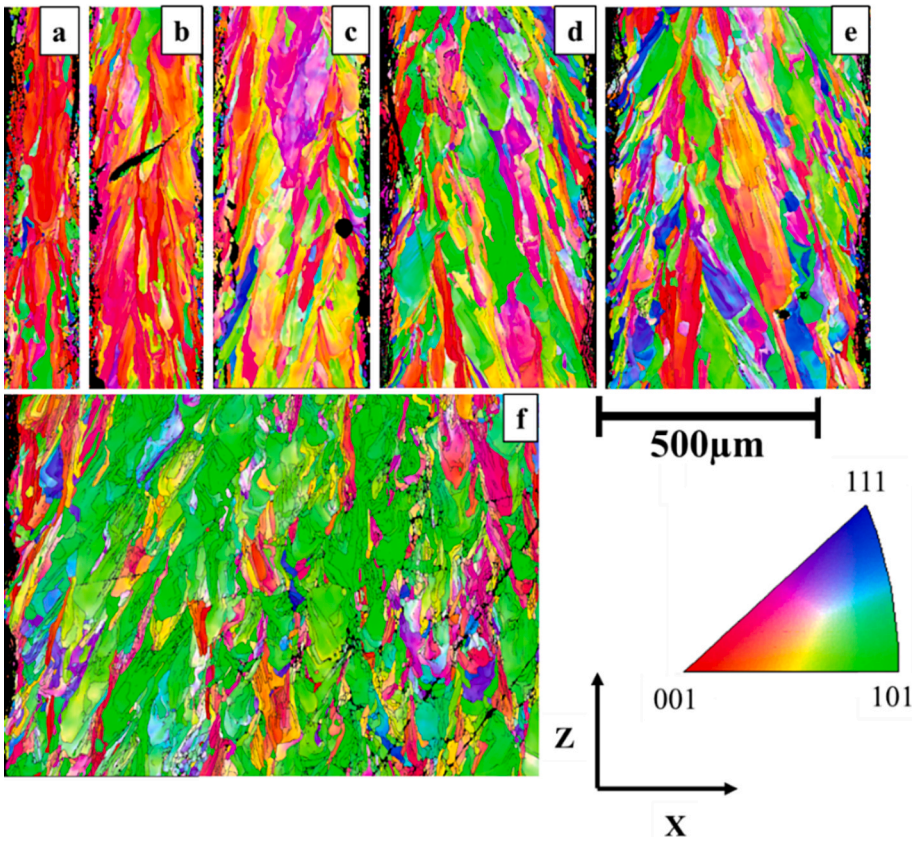

Fig. 7. Inverse pole figure maps of LB-PBF SS316L thin-walled samples subjected to HT1 conditions (1050 °C, 135 min) – XZ microstructural plane: a) 0.2 mm, b) 0.3 mm, c) 0.4 mm, d) 0.5 mm, e) 0.6 mm and f) 1.8 mm.

Table 5
Microstructural parameters for LB-PBF SS316L thin-walled samples subjected to HT1 conditions (1050 °C, 135 min).

Thickness (mm)	Grain size (μm^2)	Aspect ratio	LAB Relative Frequency	Σ3 (%)	Maximum MUD	Rx %
0.2	222	0.19	0.813	0	7.26	23.12
0.3	284	0.16	0.838	0.05	3.50	25.45
0.4	306	0.22	0.843	0.14	3.28	21.60
0.5	408	0.22	0.908	0.11	2.50	16.10
0.6	341	0.20	0.890	0.11	1.82	15.45
1.8	474	0.28	0.852	0.02	3.68	19.41

grain size increases from 1076 to 1269 μm^2, and the twinning (Σ3 boundary) percentage rises significantly from 17.09 % to 48.08 %. Additionally, the thicker samples (1 mm and 1.8 mm) show some alignment toward the <101> orientation, although MUD values in Fig. 12 suggest a largely anisotropic structure with weak microstructural texture. The reduction in texture is compounded by a reduced average MUD value of 2.3 for HT3 samples. Although alignment toward the <101> is evident in the 1 mm and 1.8 mm samples, this is a direct result of the increased sample size.

Minor variations, such as a higher population of abnormally grown grains (as shown in Fig. 11a)), may arise from localised differences in grain boundary mobility or stored energy heterogeneities prior to processing. Recrystallisation percentages are consistently high, reaching 99.73 % in the 1.8 mm sample, implying that a temperature of 1200 °C consistently produces near full recrystallisation within the LB-PBF SS316L samples across all investigated thickness (0.8–1.8 mm). Samples below 0.8 mm could not be investigated under this heat treatment due to increased oxide formation at this elevated temperature. Which ultimately led to a complete reduction in metallic material. Therefore, EBSD analysis was not feasible.

3.2. Oxide analysis

3.2.1. As-built

In addition to the microstructural findings gathered from EBSD, further imaging was recorded using the same SEM coupled with EDS analysis. However, Fig. 13b was created using the FEG-SEM. As presented in Fig. 13, the EDS analysis from the as-built 0.6 mm sample reveals a relatively low distribution of micron-scale oxides at the wall edge. Several larger particles, rich in Si, Mn and O, can be seen in more internal sub-surface locations, however the bulk of the oxides are precipitated at a nano-scale, as shown in Fig. 13b.

3.2.2. Heat-treatment 1 (1050 °C, 135 min)

Similar behaviour is shown in the HT1 samples, where the back-scattered electron (BSE) micrographs in Fig. 14a reveal the presence of oxide particles dispersed throughout the microstructure, with higher magnification images highlighting their distribution and morphology (Fig. 14b). EDS maps confirm that these oxides are primarily rich in Si and Mn, with some also containing Mo. The spatial distribution suggests that these larger oxides have formed during the LB-PBF process, i.e. within a melt pool and subsequently coarsened during heat treatment at 1050 °C. Notably, when compared to the as-built material, the nano-oxide particles have slightly coarsened, since very few smaller oxides are visible after HT. These particles (as shown in Fig. 14b) are below the resolution limit of EDS detection and do not appear in the elemental maps. Their presence, though not evidently observed, is inferred from the microstructural contrast variations, as seen in Fig. 14b. These oxides can contribute to particle pinning effects, affecting the overall microstructural stability and mobility of migrating grains.

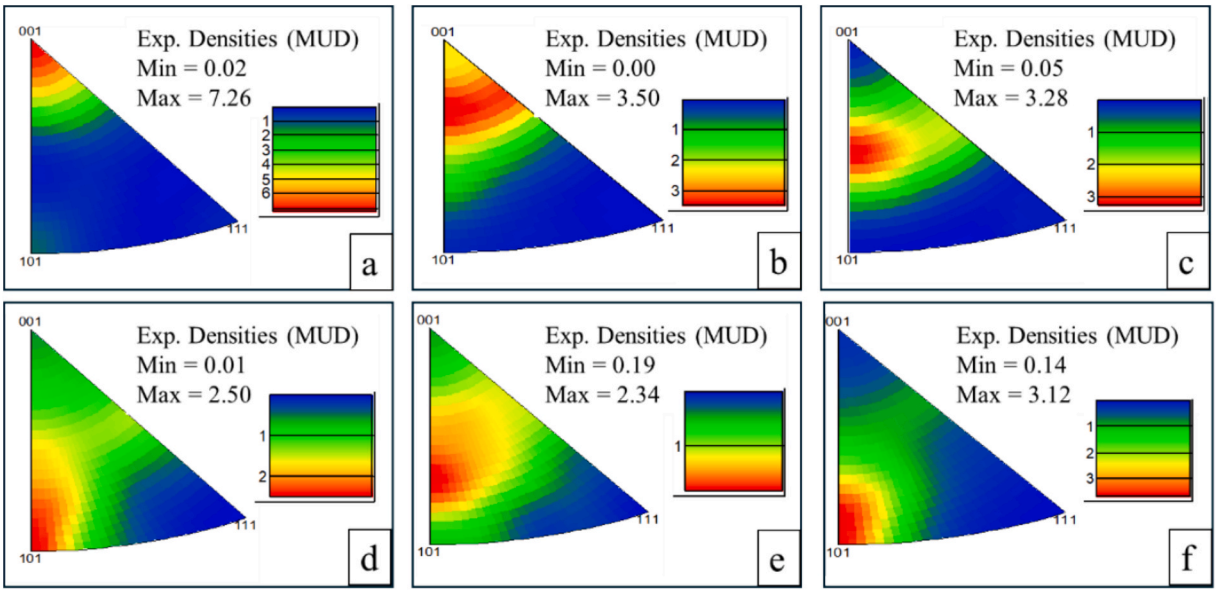

Fig. 8. Inverse pole figures of LB-PBF SS316L thin-walled samples subjected to HT1 conditions (1050 °C, 135 min) – XZ microstructural plane: a) 0.2 mm, b) 0.3 mm, c) 0.4 mm, d) 0.5 mm, and e) 0.6 mm wall edge.

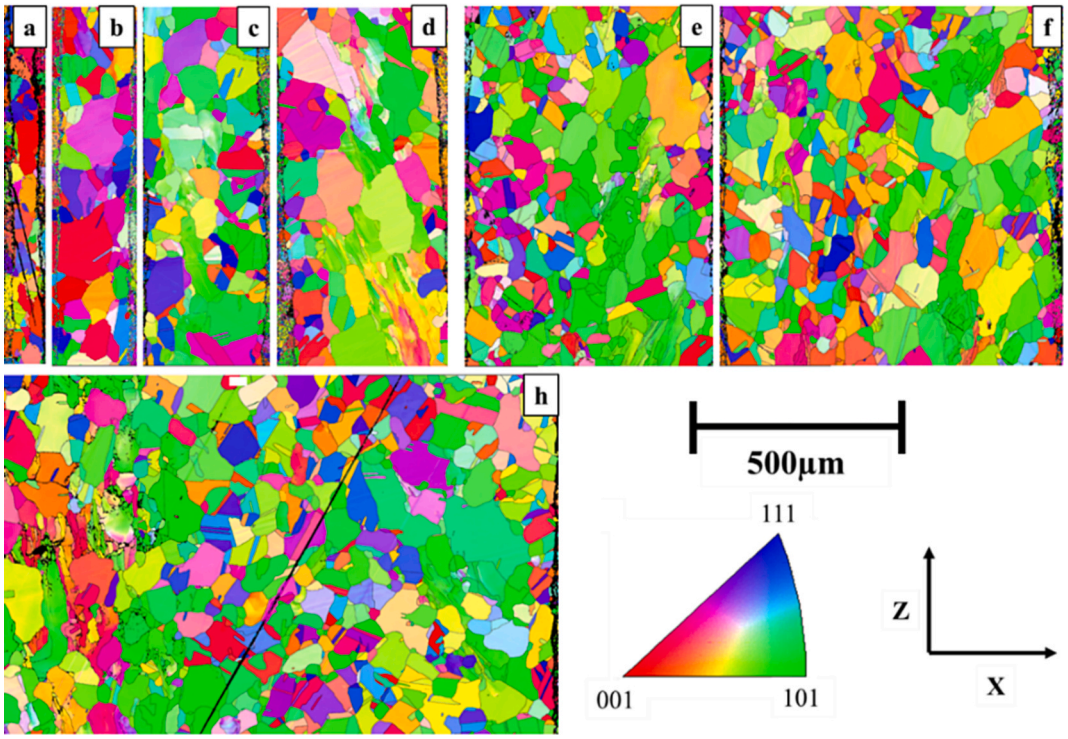

Fig. 9. Inverse pole figure maps of LB-PBF SS316L thin-walled samples subjected to HT2 conditions (1150 °C, 135 min) – XZ microstructural plane: a) 0.3 mm, b) 0.4 mm, c) 0.5 mm, d) 0.6 mm, e) 0.8 mm, f) 1 mm, g) 1.8 mm.

3.2.3. Heat-treatment 2 (1150 °C, 135 min)

At an annealing temperature of 1150 °C, the microstructure exhibits evidence of significant oxide coarsening, with oxides forming/precipitating along the boundaries of non-recrystallised AM grains. The BSE micrograph (Fig. 15a) presents a distinct contrast between recrystallised and unrecrystallised grains, highlighting the impact of oxide particle distribution on the recrystallisation process. The unrecrystallised grain remains elongated, indicative of the original solidification structure from LB-PBF processing, whereas the surrounding recrystallised regions display a more equiaxed morphology.

EDS elemental mapping in Fig. 15 suggests that the oxides rich in Si and Mn, which were initially fine and dispersed in the as-built condition, have now coarsened and segregated along grain boundaries. This behaviour aligns with the expected role of oxide pinning during annealing, where oxides initially inhibit grain boundary movement but eventually coarsen at higher temperatures. This potentially reduces their effectiveness as recrystallisation inhibitors, supporting and justifying the sluggish recrystallisation at 1150 °C. As such, the presence of the oxides has significantly hindered grain boundary migration. Therefore, higher temperatures are required to possibly dissolve oxides or

Table 6
Microstructural parameters for LB-PBF SS316L thin-walled samples subjected to HT2 conditions (1150 °C, 135 min).

Thickness (mm)	Grain size (μm^2)	Aspect ratio	LAB Relative Frequency	Σ3 (%)	Maximum MUD	Rx (%)
0.3	386	0.38	0.847	1.65	5.66	99.9
0.4	1050	0.37	0.280	26.7	2.95	93.4
0.5	895	0.37	0.449	19.7	3.10	85.7
0.6	918	0.29	0.704	9.26	2.02	72.2
0.8	827	0.40	0.547	17.75	3.01	89.8
1	879	0.39	0.402	23.01	2.58	90.8
1.8	802	0.36	0.666	21.09	2.22	86.1

increase atomic mobility, to facilitate boundary migration. Although oxides typically precipitate at grain boundaries, there are a large number of particles that are dispersed in intragranular locations, as shown in Fig. 15.

3.2.4. Heat-treatment 3 (1200 °C, 135 min)

At the highest annealing temperature of 1200 °C, the microstructure exhibits a more uniform grain structure with evidence of extensive recrystallisation. The backscattered micrograph in Fig. 16 reveals that oxide particles distributed both within grains and along grain boundaries, suggesting that some oxides have coarsened and remained trapped within grain, whilst others have migrated and segregated at grain boundary locations.

Table 7
Microstructural parameters for LB-PBF SS316L thin-walled samples subjected to HT3 conditions (1200 °C, 135 min).

Thickness (mm)	Grain size (μm^2)	Aspect ratio	LAB Frequency	Σ3 (%)	Maximum MUD	Rx %
0.8	1076	0.42	0.474	17.09	1.99	98.37
1	1249	0.39	0.339	21.25	2.78	98.82
1.8	1269	0.36	0.15	48.08	2.21	99.73

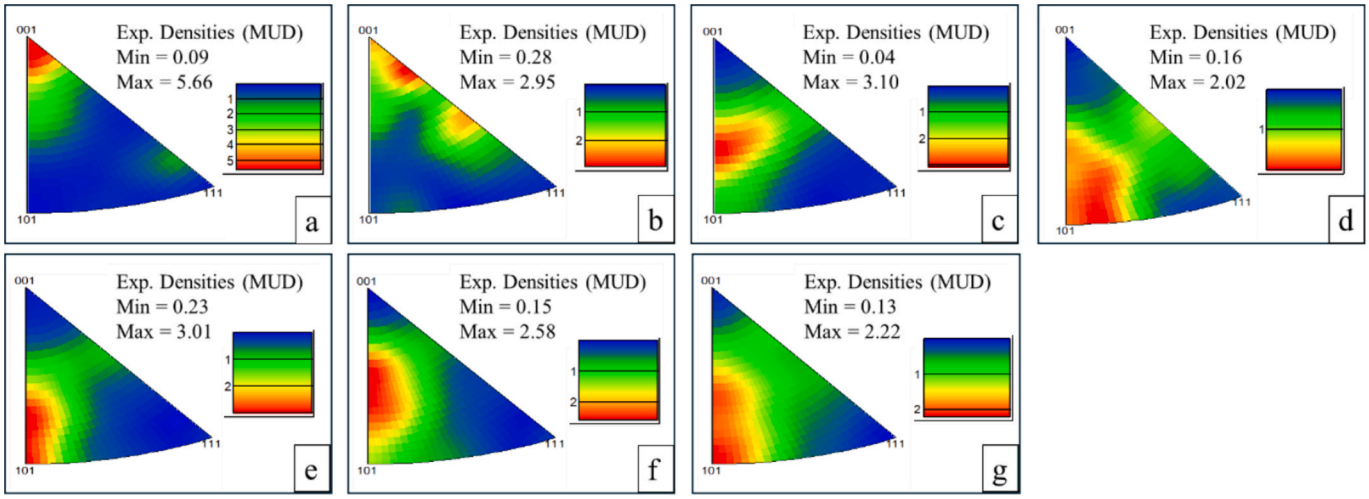

Fig. 10. Inverse pole figures of LB-PBF SS316L thin-walled samples subjected to HT2 conditions (1150 °C, 135 min) – XZ microstructural plane: a) 0.2 mm, b) 0.3 mm, c) 0.4 mm, d) 0.5 mm, e) 0.6 mm, f) 0.8 mm, g) 1 mm and h) 1.8 mm wall edge.

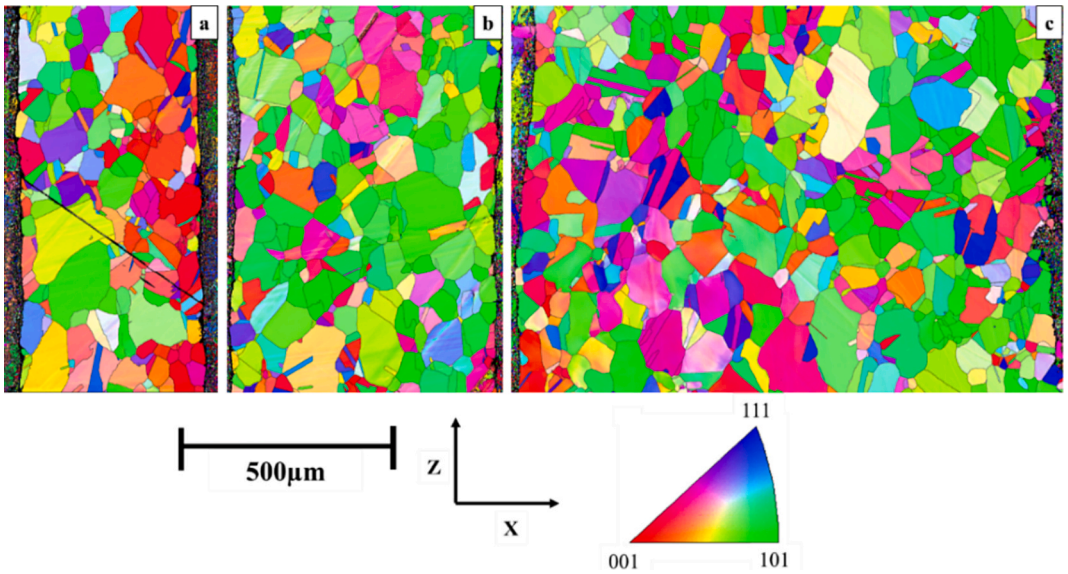

Fig. 11. Inverse pole figure maps of LB-PBF SS316L thin-walled samples subjected to HT3 conditions (1200 °C, 135 min) – XZ microstructural plane: a) 0.8 mm, b) 1 mm and c) 1.8 mm.

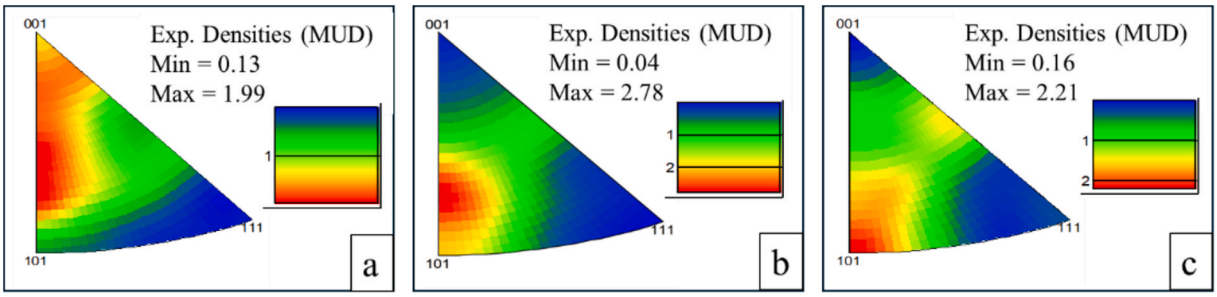

Fig. 12. Inverse pole figures of LB-PBF SS316L thin-walled samples subjected to HT3 conditions (1200 °C, 135 min) – XZ microstructural plane: a) 0.8 mm, b) 1 mm and c) 1.8 mm.

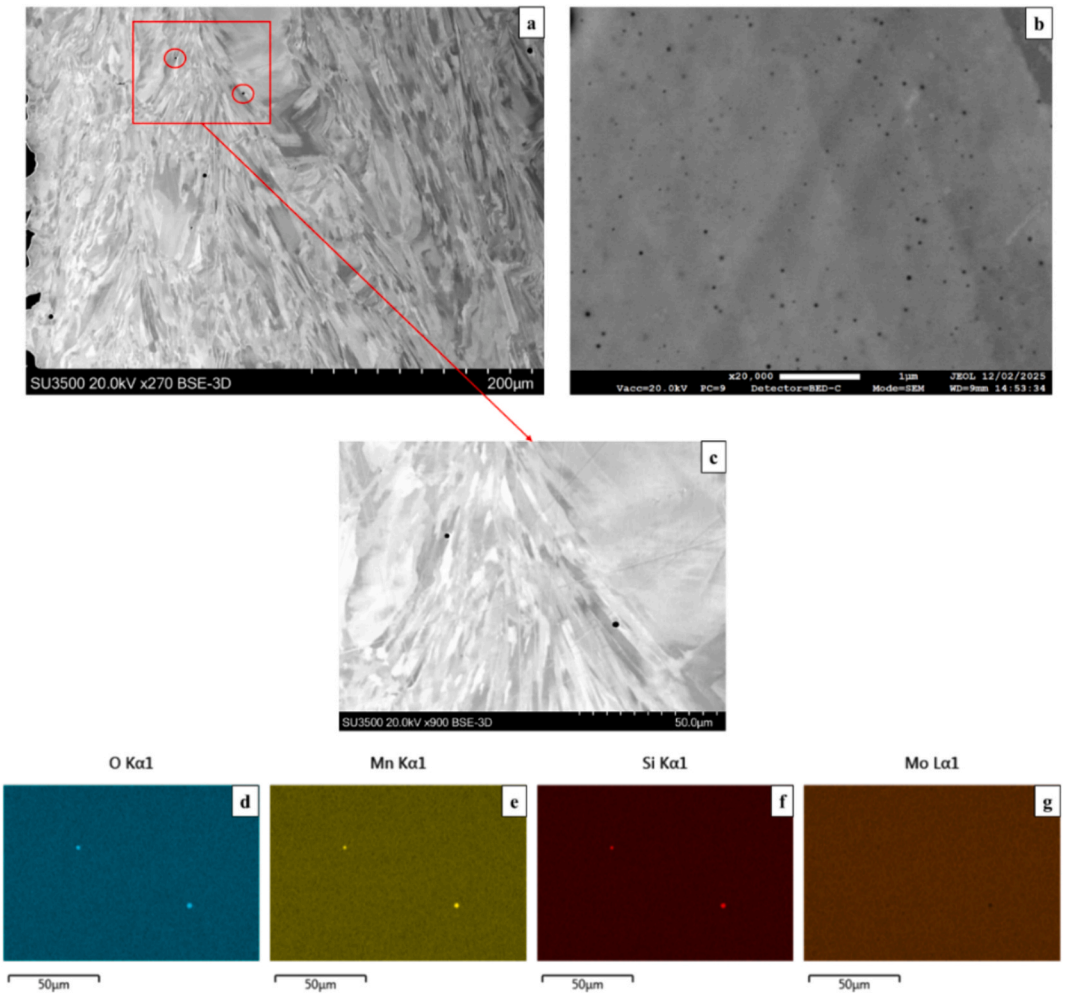

Fig. 13. As-built thin-walled LB-PBF SS316L samples – XZ microstructural plane: a) Backscattered image of the wall edge of 0.6 mm thick sample, b) High magnification image from the central part of sample, showing a fine distribution of nano-oxides, c) EDS mapped area of large features with corresponding elemental maps d) O map, e) Mn map, f) Si map and g) Mo map.

The presence of intragranular oxides could indicate that some particles were either engulfed by growing recrystallised grains or remained stable within the matrix, contributing to potential strengthening effects. In contrast, the accumulation of grain boundary oxides may influence grain boundary mobility, either acting as pinning sites that slow grain growth or, at higher temperatures, becoming more mobile and redistributing along the boundaries, which is evidently seen in Fig. 16. The uniform grain structure observed in this condition suggests that recrystallisation has progressed significantly, reducing the fraction of non-recrystallised grains seen at lower annealing temperatures. However, very small, non-recrystallised grains are still present in the microstructure and are essentially pinned in place, due to Zener pinning forces, having been completely surrounded by oxide particles.

Fig. 17a illustrates that although full recrystallisation was produced in the HT3 1 mm thin-walled sample, a small number of non-recrystallised AM grains are present and pinned in place, not only by the recrystallised grains surrounding them but the distribution of oxides on their corresponding grain boundary. These oxides looked to have been dragged by the migrating boundaries of the recrystallised grains either side.

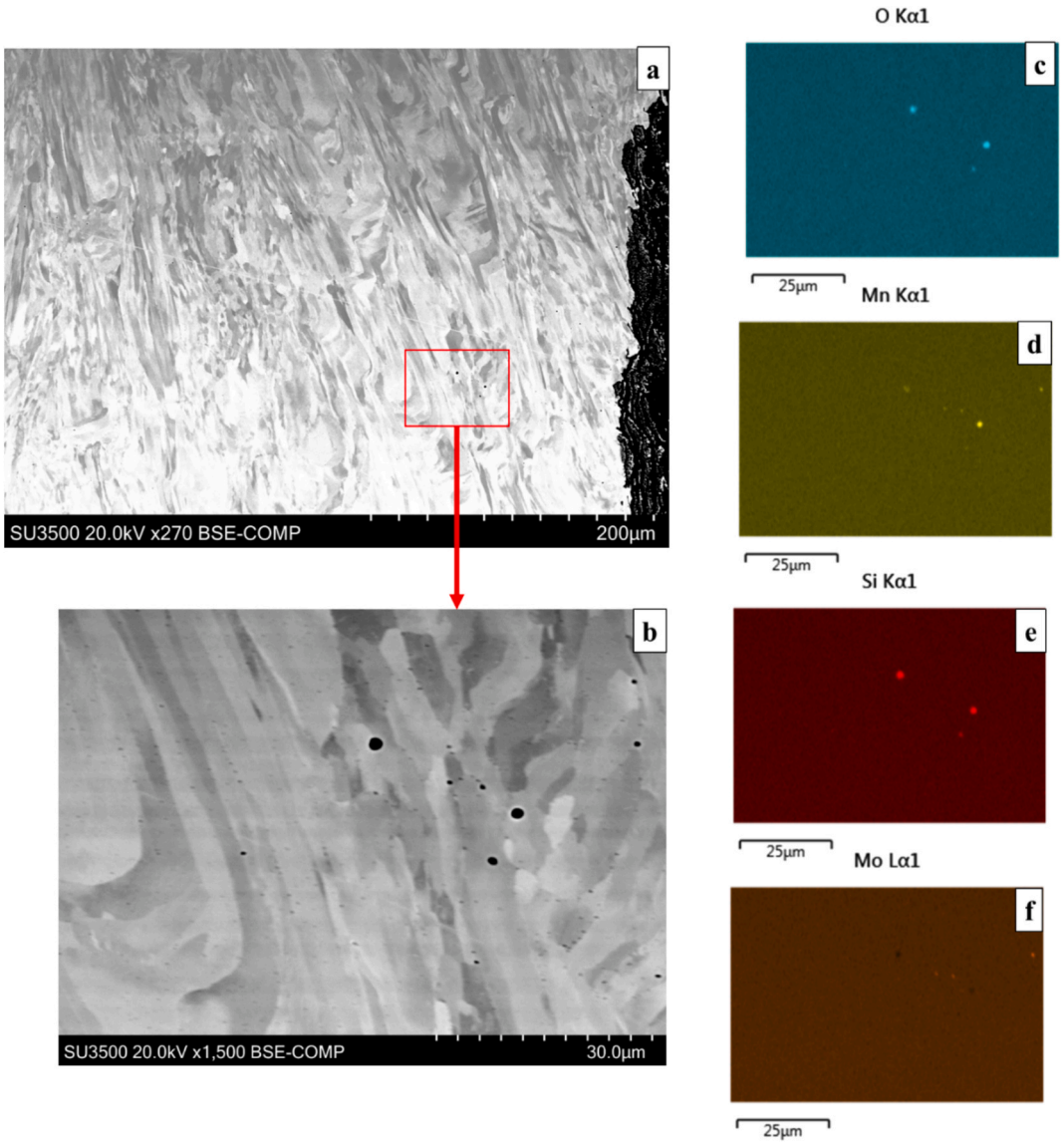

Fig. 14. LB-PBF SS316L thin-walled samples subjected to HT1 conditions (1050 °C, 135 min) – XZ microstructural plane: a) Backscattered image of the wall edge of 0.6 mm thick sample, b) EDS mapped area of large features with corresponding elemental maps c) O map, d) Mn map, e) Si map and f) Mo map.

3.2.5. Zener pinning and driving pressure in recrystallisation

Oxide distribution analysis was conducted on each HT condition to calculate relevant and representative distribution maps (Fig. 18) and the subsequent Zener pinning pressures. While distribution and volume fractions were measured from different area sizes, each sampled area was considered to accurately represent each LB-PBF SS316L condition sufficiently. However, due to potential microstructural inhomogeneity in AM SS316L, the absolute values may carry local variation. Evidently, a systematic increase in average particle radius can be seen with increasing heat treatment temperature.

The Zener pinning pressure (P_z), which depends on the particle radius (r, in m), volume fraction (f, as a ratio) and grain boundary energy (γ, in J/m^2) can be described by the following expression [19,38]:

$$P_z = \frac{3V_f\gamma_{GB}}{2r} \quad (1)$$

Using a literature cited value for γ of 0.668 J/m^2 for SS316L [34,39], in the as-built condition, the average particle radius was 0.0178 µm with a volume fraction of 0.533 %, resulting in a pinning pressure of approximately 0.31 MPa. At 1050 °C, the average radius increased to 0.0747 µm, and the volume fraction was 0.41 %, resulting in a lower pinning pressure of 0.056 MPa, approximately 18 % of the as-built value. Heat treatment at 1150 °C (HT2) led to further coarsening (0.2609 µm) and a reduction in volume fraction (0.293 %), which subsequently lowered the pinning pressure to 0.0113 MPa. Finally, at 1200 °C (HT3), particles coarsened further to 0.4392 µm, with volume fraction increasing again to 0.842 %, yielding a slightly higher pinning pressure of 0.019 MPa.

With HT1 exhibiting a lower pinning pressure of 0.0551 MPa at 1050 °C compared to as-built of 0.31 MPa, the driving pressure must have a lower value, which would explain the negligible impact on recrystallisation. The driving pressure (P_D) for static recrystallisation can be estimated using the stored deformation energy per unit volume due to dislocations [40]. The expression is shown below:

$$P_D = \frac{1}{2}\rho G b^2 \quad (2)$$

Where ρ is the dislocation density, which in this case can be inferred from the average GND density displayed in Table 4 for as-built LB-PBF SS316L (1.30 × 10^{14} /m^2), G is the shear modulus of ~77 GPa and b is the burgers vector magnitude for 316L stainless steel of 0.2541 nm, as calculated in previous research [41]. The P_D was calculated to be 0.323

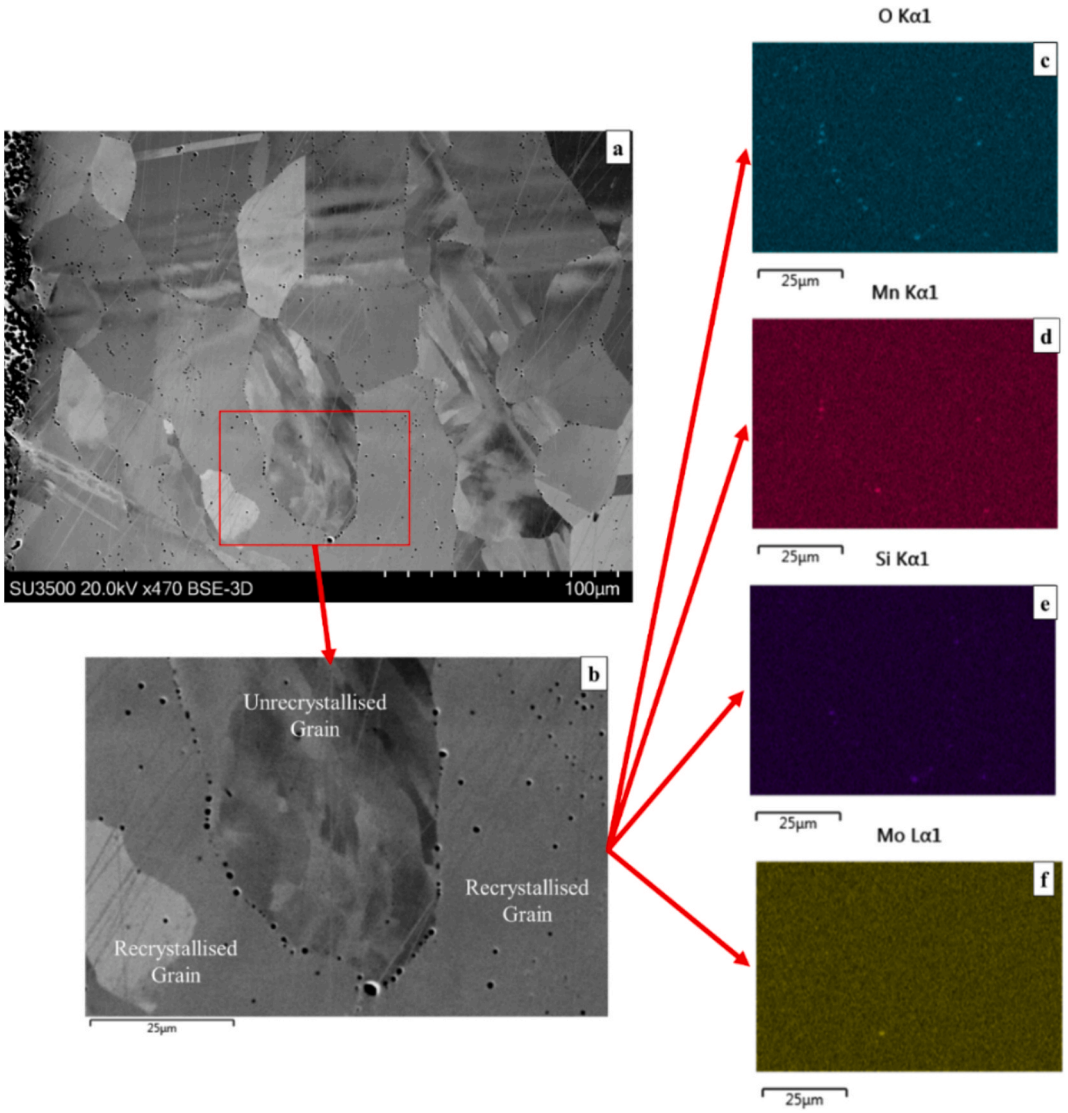

Fig. 15. LB-PBF SS316L thin-walled samples subjected to HT2 conditions (1150 °C, 135 min) – XZ microstructural plane: a) Backscattered image of 0.6 mm sample, b) EDS mapped area of AM grain surrounded by particles with corresponding elemental maps c) O map, d) Mn map, e) Si map and f) Mo map.

MPa, similar to literature values [34], however significantly higher than the particle pinning pressure. Therefore other parameters must influence the recrystallisation kinetics.

3.3. Mechanical properties

Fig. 19 presents the hardness results generated on the thin-walled samples across the four HT conditions. To note, no reliable, relative hardness values were possible in the 0.2 mm samples subjected to the various heat treatment procedures due to severe oxidation effects. This was also the case for 0.3 mm sample under HT2 conditions, and any thickness below 0.8 mm in the case of HT3.

In the as-built state, the mean hardness remains relatively consistent across sample thicknesses from 0.2 mm to 0.6 mm, ranging between 210.74 Hv and 244.33 Hv. A slight decrease in hardness is observed from 0.2 mm to 0.5 mm, with a notable dip at 0.5 mm (210.74 Hv), probably due to scatter, before increasing again at 0.6 mm (244.33 Hv). The 0.5 mm sample shows the highest inconsistency, with a standard deviation of 30.82. This is unsurprising when considering the microstructural morphology of this sample, as presented in Fig. 3d). As can be seen, this sample starts to show a higher propensity to the <101> orientation when compared to the thinner wall thicknesses (0.2–0.4 mm) which are seen to be more oriented towards <001>. However, in the 0.6 mm wall thickness, <101> oriented grains are more prominent, as reflected by the sample exhibiting the lowest SD of 10.32.

After heat treatment at 1050 °C (HT1), the hardness decreases across all thicknesses, likely due to grain growth effects. Hardness values drop from 215.13 Hv at 0.3 mm to 185.68 Hv at 0.5 mm, with a slight increase to 190.42 Hv for the 0.6 mm sample. The 0.3 mm sample shows the greatest variation, with a standard deviation of 23.54 and a hardness value range of 81.61 Hv, highlighting the lack of homogeneity. In contrast, the 0.4 mm and 0.5 mm samples exhibit lower standard deviation values of 8.29 and 8.17, respectively, indicating a more uniform behaviour. The lowest range and standard deviation is observed in the 1.8 mm sample exhibiting values of 16.89 Hv and 6.11, respectively.

At 1150 °C (HT2), the hardness behaviour shows larger variation, with a sharp increase in hardness seen in the 0.3 mm sample (281.99 Hv), significantly higher than other samples. For thicker samples (0.4 mm to 0.6 mm), the hardness progressively decreases from 235.81 to 206.50 Hv. This substantial increase in hardness for the 0.3 mm sample may be attributed to the decrease in grain size throughout the microstructure at this temperature. Variability is highest in the 0.3 mm and 0.4 mm samples, showing the highest standard deviation, while the 0.5 mm and 0.6 mm samples show more consistent hardness, with lower

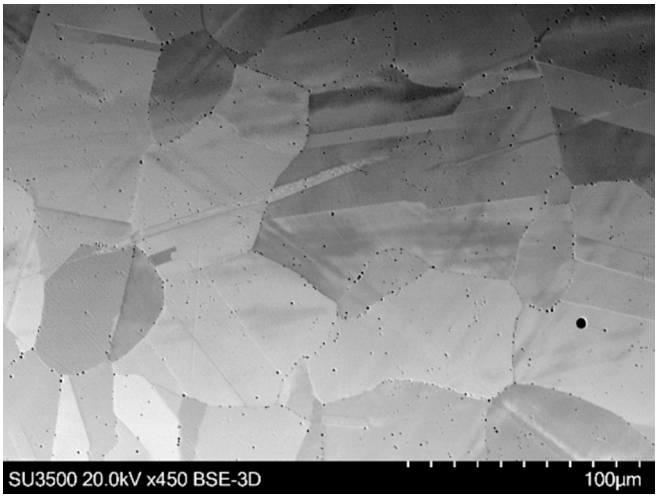

Fig. 16. Backscattered image of LB-PBF SS316L 1 mm thin-walled sample subjected to HT3 conditions (1200 °C, 135 min) – XZ microstructural plane. Image reveals a significant distribution of particles precipitated along grain boundaries and within newly recrystallised grains.

standard deviations. The highest range in hardness for the 0.4 mm sample (62.88 Hv), with the 0.5 mm sample (50.67 Hv) slightly below, indicating some heterogeneity in the microstructure, likely resulting from the uneven recrystallisation throughout the sample. The presence of 'abnormally' grown grains will undoubtedly influence these measures, due to the hardness indent only bearing a force of 50 g, which unknowingly could be testing a single grain.

For samples heat treated at 1200 °C (HT3), the hardness values generally show an increase with sample thickness. The 0.8 mm sample has an average hardness of 221.53 HV with low variability (standard deviation 10.25), while the 1 mm sample shows a slightly lower average hardness of 207.18 HV but with increased spread. The 1.8 mm sample exhibits the highest average hardness at 245.22 HV and the greatest variability, indicated by the highest range of all tested samples, as given in Table 6. These trends suggest that thicker samples from HT3 maintain a hardness level and associated variability closer to those observed in the corresponding as built samples. The increased presence of abnormally grown grains is likely the major contributing factor for this difference, as the 50 g force will undoubtably be testing a greater number of single grains in the thicker samples.

A non-uniform relationship was seen when considering grain size and hardness properties, as depicted in Fig. 20. Again, there is no strong correlation between the two parameters, apart from illustrating that grain size generally increases with an increase in heat treatment.

4. Discussion

Previous studies have shown that post fabrication heat treatments at temperatures of 800–1200 °C can fully recrystallise austenitic LB-PBF SS316L microstructures [28,34,42]. This study failed to produce full recrystallisation in thin-walled samples at 1050 °C or 1150 °C, apart from applying HT2 in the 0.3 mm sample. However, caution should be taken when assuming that full recrystallisation has taken place in this sample since only a reduced material cross-section remains due to oxidation from the HT regime. HT3 proved to reproduce sufficiently high recrystallisation values >98 % across a range of investigated thicknesses with small, non-recrystallised AM grains pinned in-between newly recrystallised grains.

Fig. 21 presents the effect of heat treatment and wall thickness on the recrystallisation behaviour on the LB-PBF SS316L samples. The figure illustrates that in the HT2 samples, recrystallisation levels fall with an increasing sample thickness to ~70 %, however at 0.8 mm and 1 mm, it is clear that recrystallisation significantly increases by around ~20 %.

At intermediate wall thicknesses between 0.6 mm and 0.8 mm, the microstructure has a central 'band' of heavily textured grains, preferential to the <101> orientation, which could potentially contribute to the delayed recrystallisation observed. For the HT3 samples however, consistent results across each of the alternative wall thicknesses are found, exhibiting high levels of recrystallisation near ~100 %. The scatter from the GOS calculations may be the reason for the calculations sitting just below 100 %. Additionally, scratching of the sample due to oxide break-off during polishing may falsely increase the GOS of certain grains, potentially causing 'homogeneous' grains to be misinterpreted as uncrystallised during calculations. Nonetheless, Fig. 11 demonstrates that all mapped grains are newly recrystallised and it can safely be assumed that 100 % recrystallisation is being replicated for all samples subjected to the HT3 parameters.

The results from the three heat treatment (HT) cycles at 1050 °C, 1150 °C and 1200 °C reveal several important findings worth discussing. Notably, no significant microstructural changes were observed following the 1050 °C heat treatment; partial recrystallisation occurred at 1150 °C; and the microstructure was near full recrystallisation at 1200 °C, for the range of wall thicknesses investigated. Previous studies have shown that the driving force for recrystallisation is directly related to the geometrically necessary dislocation (GND) density in the initial LB-PBF microstructure [26,27]. In AM materials, dislocation densities are influenced by the cooling rate and the geometrical constraints of the melt pool [43]. Therefore, cyclic heating and cooling in localised zones during processing lead to the formation of dislocations, creating residual stresses that accommodate local expansion or contraction. When these stresses induce plastic deformation, dislocations accumulate into cellular patterns. These dislocations, known as GNDs, facilitate local lattice rotations and accommodate changes in shape or orientation, particularly during solidification. Therefore, a higher dislocation density would undoubtedly increase stored energy throughout the microstructure, promoting a faster or more sufficient recrystallisation. This phenomena is consistent with previous research where a higher dislocation density was obtained in LB-PBF SS316L compared to the same material manufactured through a directed energy deposited AM process [7]. However, the previous findings reporting the GND density has solely been researched and linked to bulkier LB-PBF SS316L components, with little to no mention of thin-walled microstructures.

As presented in Fig. 5 and Table 4, it is evident that an increased GND density does not lead to increased recrystallisation levels. For example, the as-built 1.8 mm thick sample has the highest GND value of $1.3910^{14}/m^2$, yet only exhibits a recrystallisation level of 86.1 % at 1150 °C. Fig. 22 supports the ideology that areas of increased stored energy do not necessarily lead to the nucleation of recrystallisation, as stated by Lee [44].

For context, as part of this study, a wrought equivalent of SS316L was also analysed and was found to exhibit a GND of $0.22\ 10^{14}/m^2$. Table 4 shows the GND density values of all sample thicknesses in the as-built condition and reveals that the 1.8 mm sample exhibits the highest GND density, however, as shown in Fig. 21 for HT2, the 1.8 mm wall thickness does not achieve the highest percentage of recrystallisation. Although reports [26,27] suggest GND density is the driving force for recrystallisation, other factors such as oxide precipitation and dispersion may have a much greater overall effect on the microstructure to mitigate the GND density.

Given the lack of correlation between GND density and recrystallisation, other parameters need to be considered. One such feature is the presence of LAB and HAB frequency, as HABs are a well-known preferential site of nucleation for recrystallisation [19]. Also, they possess higher mobility than LABs, therefore being important for the growth mechanism [19]. Nonetheless, in this investigation the HAB frequency does not have any correlative effects on the recrystallisation, as shown in Fig. 23. Here, across all thickness values, the HAB and LAB frequency have been compared against the recrystallisation percentage, exhibiting

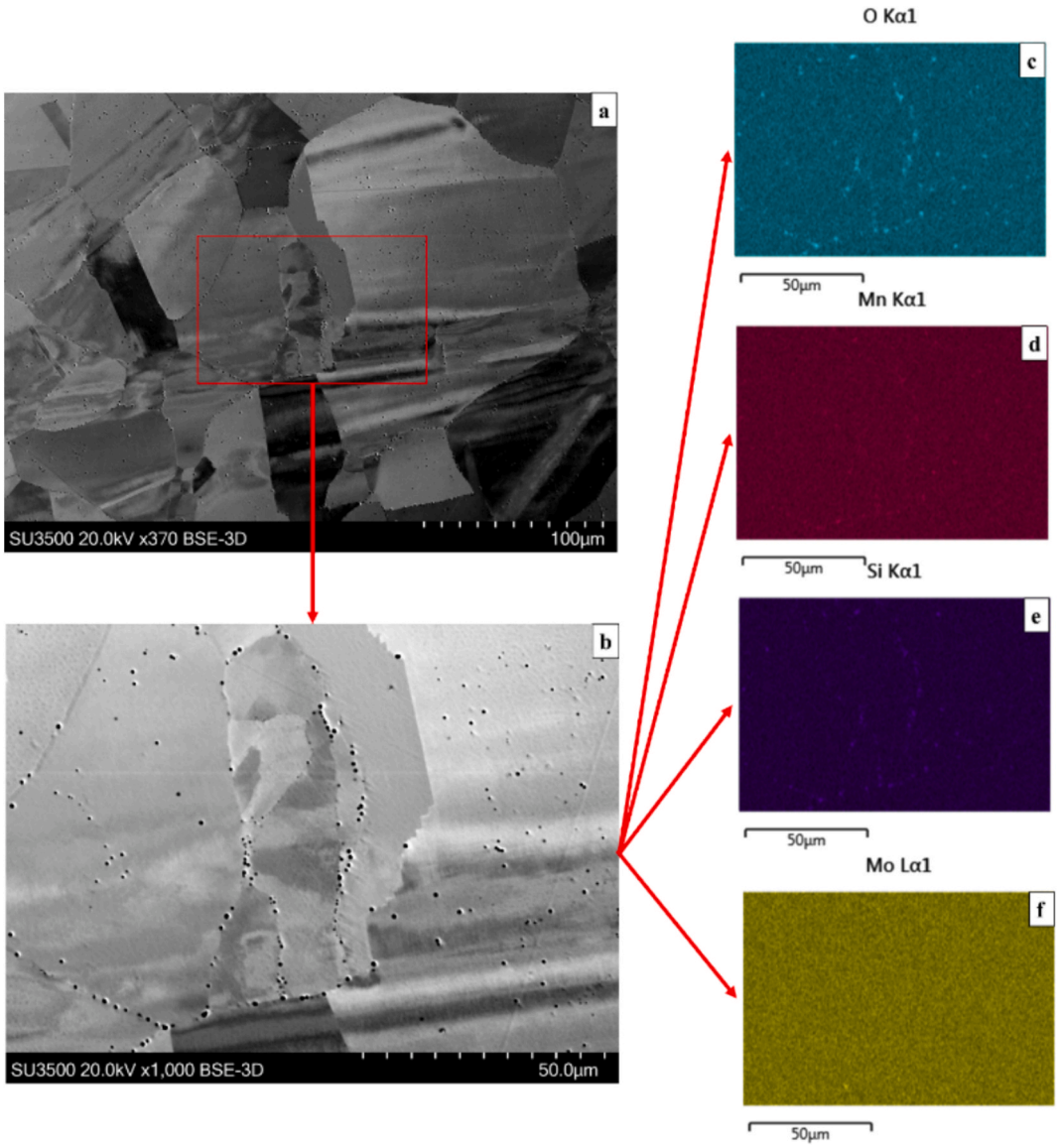

Fig. 17. LB-PBF SS316L thin-walled samples subjected to HT3 conditions (1200 °C, 135 min) – XZ microstructural plane: a) Backscattered image of 1 mm sample, b) EDS mapped area of non-recrystallised AM grain surrounded by particles with corresponding elemental maps c) O map, d) Mn map, e) Si map and f) Mo map.

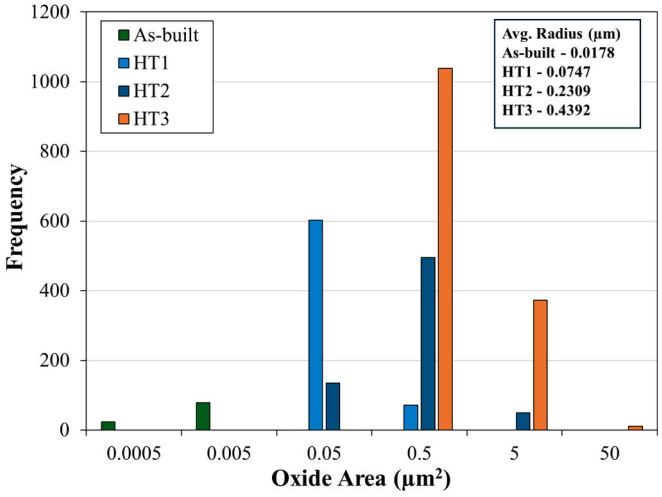

Fig. 18. Comparison of the oxide distribution for as-built, HT1, HT2 and HT3 conditions.

minimal correlation between these microstructural parameters.

The observed lack of direct correlation between Vickers hardness and microstructural parameters, as shown in Fig. 19, can be attributed to several interrelated factors. Firstly, oxide dispersion strengthening [37] plays a significant role in the annealed samples, where the distribution of oxide particles act as effective barriers to dislocation motion, thereby contributing to hardness independent of grain size or recrystallisation fraction. To characterise this would be very difficult and outside of the study's limitations. Secondly, residual stress relief is not uniform across varying wall thicknesses, resulting in inconsistencies in recrystallisation fractions. Likewise, the differing localised areas of recrystallisation evidently lead to spatial heterogeneity in the hardness values that do not necessarily align with microstructural changes. Additionally, the relatively low indentation force used during testing likely emphasised these local variations; the indenter tip may have indented directly on hard, brittle oxide particles, which are known to significantly increase local hardness through oxide dispersion strengthening.

Nucleation is defined as the process in which dislocations rearrange within a deformed/recovered structure, forming regions of low dislocation density that contain at least one high-angle grain boundary.

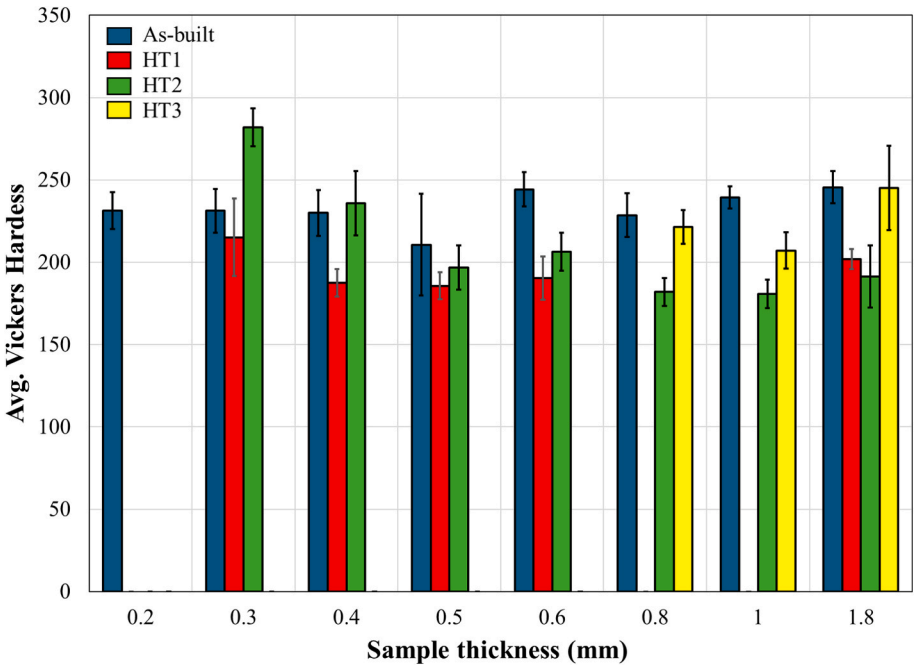

Fig. 19. Effect of heat treatment and wall thickness on the hardness properties of thin-walled LB-PBF SS316L samples in the as-built and heat treated (HT1–HT3) conditions.

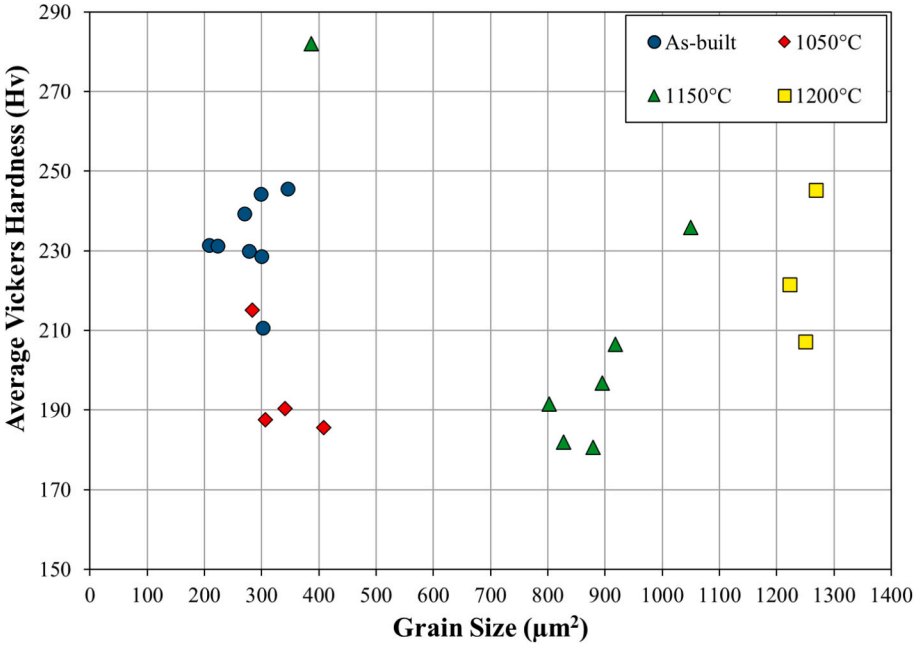

Fig. 20. Effect of heat treatment and grain size on the hardness properties of thin-walled LB-PBF SS316L samples in the as-built and heat treated (HT1–HT3) conditions.

These low dislocation density regions have the potential to rapidly grow and consume the surrounding deformed matrix [19], in this case being the columnar-like structure of the LB-PBF samples. It is well known that nucleation can occur at different sites in a deformed microstructure [19]. In this study, the as-built LB-PBF SS316L is subsequently deformed with a high energy state for recrystallisation to nucleate. However, as already discussed, Fig. 15 proves higher stored energy through GND density does not lead to high recrystallisation levels. In this study, nucleation in the thin-walled samples would occur either by the movement of pre-existing HABs or the formation of new ones, assuming that strain-induced boundary migration (SIBM) is the primary nucleation mechanism for LB-PBF SS316L during static recrystallisation. This mechanism describes the formation of recrystallisation nuclei through the bulging of a dislocation-free subgrain into a grain with higher stored energy [19], possibly due to the presence of geometrically necessary dislocations (GNDs) and LAB. The driving force for the formation of a recrystallisation nucleus is the stored energy difference, ΔE, between two neighbouring grains sharing a HAB. Once a nucleus reaches a critical size, it begins to grow. The existence of these nuclei suggests that nuclei precursors, or embryos, must already be present in the as-built LB-

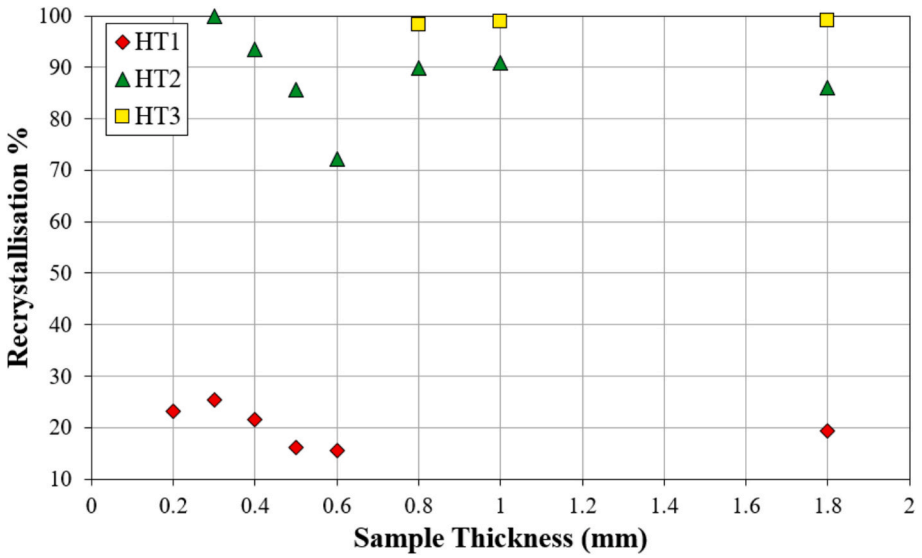

Fig. 21. Effect of heat treatment and wall thickness on the recrystallisation behaviour of thin-walled LB-PBF SS316L samples in the as-built and heat treated (HT1-HT3) conditions.

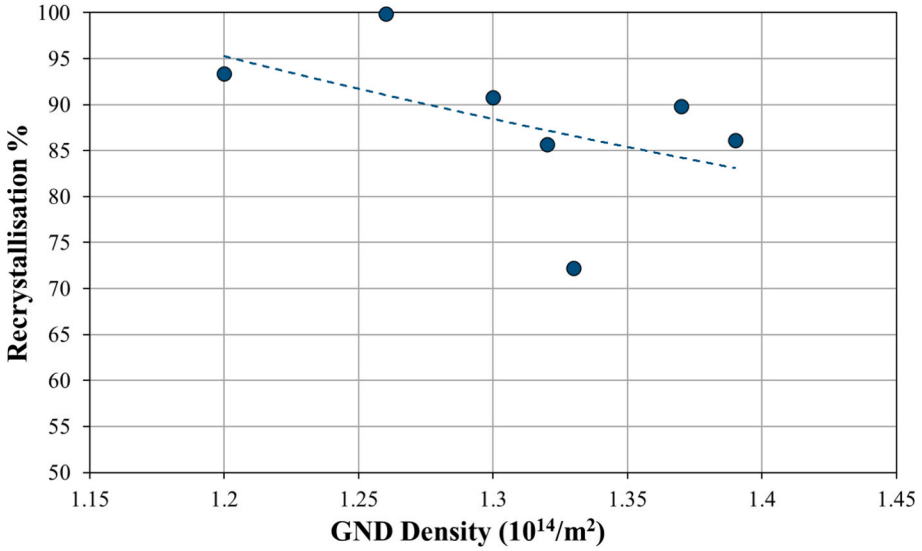

Fig. 22. The correlation between GND density and recrystallisation % of samples subjected to HT 2 conditions for all wall thicknesses for LB-PBF SS316L.

PBF structure. For an embryo to become a fully active nucleus, it must grow into the deformed matrix. As supported in Fig. 22, the presence of increased GND density does not lead to higher recrystallisation levels. Therefore, the sluggish recrystallisation is directly linked to the strong particle pinning within the LB-PBF 316L thin −walled material, as illustrated in section 3.2.

During annealing, oxide particles undergo Ostwald ripening and coarsening [45]. When a migrating boundary is pinned, its movement is temporarily halted while the particles rapidly coarsen through grain boundary diffusion. Once these particles reach a critical size, the pinning effect weakens, allowing the boundary to unpin and resume movement. This process leaves behind coarse particles within the recrystallised grains, forming a distinct pattern that reflects the previous locations of the grain boundaries. As such, these Si/Mn oxides, which form during the annealing of LB-PBF SS316L, play a crucial role in inhibiting recrystallisation by pinning grain boundaries and restricting their mobility. As annealing increases atomic mobility, Si and Mn diffuse toward grain boundaries and react with residual oxygen, forming stable oxides such as $MnSiO_3$ and Mn_2SiO_4. Due to their high-energy state, these oxides preferentially nucleate at grain boundaries, where they exert a Zener pinning effect [46] that inhibits boundary migration. Over time, Ostwald ripening causes smaller oxide particles to dissolve and redeposit onto larger ones, leading to oxide coarsening [23]. As these oxides grow, their pinning effect diminishes, as once they surpass a critical size, they can no longer effectively impede boundary motion, allowing previously pinned boundaries to become mobile again.

This delayed boundary movement can result in abnormal grain growth [47] rather than uniform recrystallisation, depending on the heat treatment conditions. In this study, abnormal grain growth was observed in the HT2 and HT3 conditions, as shown in Figs. 9 and 11. This occurs when a small subset of grains expand significantly more than their surroundings, disrupting uniform grain size distribution. It is driven by variations in boundary mobility and stored energy among grains [48]. In the presence of coarsened Si/Mn oxides, once boundaries unpin, grains with higher mobility rapidly consume their neighbouring grains, creating a non-uniform microstructure. Thus, annealing LB-PBF SS316L samples induces a stop-and-go boundary migration mechanism, where grain boundaries are periodically pinned and unpinned due

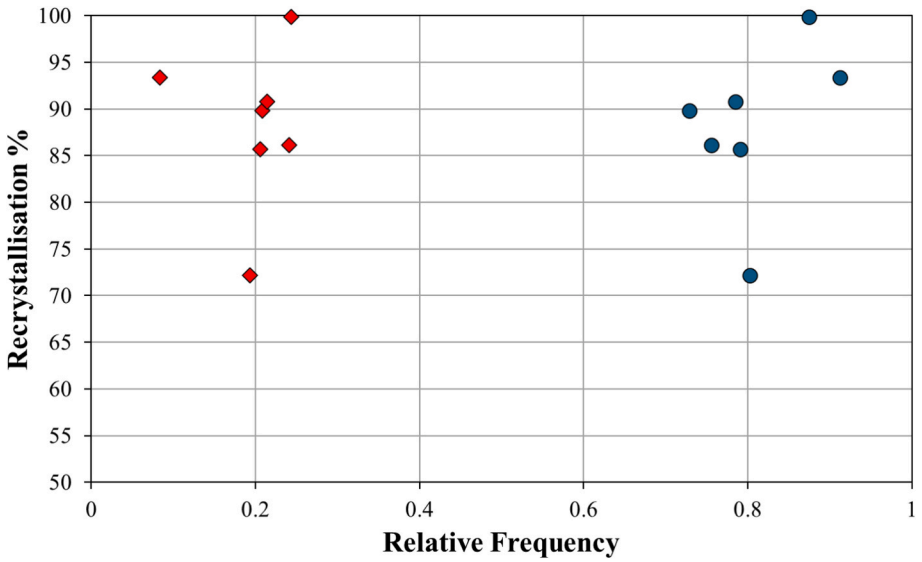

Fig. 23. Correlation between recrystallisation %, at 1150 °C, with low angle boundary (LAB = misorientation (2–15°)) and high angle boundary (HAB = misorientation >15°) frequency – heat treated at 1150 °C.

to Ostwald ripening and Zener pinning effects.

Previous studies have calculated the driving force generated by grain boundary migration, finding it to be several times greater than the gravitational force acting on inclusions. This significant difference allows oxides to be dragged along as boundaries migrate [25]. The mobility of oxide particles is strongly size-dependent, with smaller particles exhibiting much higher mobility. Consequently, the nanosized oxides present in as-built LB-PBF SS316L (seen in Fig. 13b) possess relatively high mobility and can be directly dragged through volume diffusion of the matrix atom, Fe [25,49].

The schematic in Fig. 24, adapted from Deng et al. [30] illustrates the interaction between a migrating high-angle boundary and oxide particles in LB-PBF SS316L. During recrystallisation, grain boundary migration is initiated by the nucleation of new grains, which form to reduce stored energy or grain boundary energy. As the boundaries move, they drag oxides along, leading to their accumulation at grain boundaries [25]. Smaller oxides dissolve, and their atoms diffuse toward larger oxides due to the shorter diffusion paths, with grain boundaries acting as "diffusion highways" that accelerate this process. This results in oxide growth at grain boundaries, as shown in Figs. 15a and 16.

As grain size increases, the driving force for boundary migration decreases. Larger oxides eventually detach from the boundaries, while smaller ones continue to be transported. Migration ultimately ceases once the driving force becomes insufficient, leaving oxides concentrated at grain boundaries at certain stages of recrystallisation. Over time, this fraction diminishes as grain size increases. However, due to the high diffusion rates along grain boundaries, oxides located at boundaries tend to remain larger than those within the grains. Fig. 25 provides an insight to this phenomenon, showing the oxide dispersion in HT2 0.6 mm thin-walled sample.

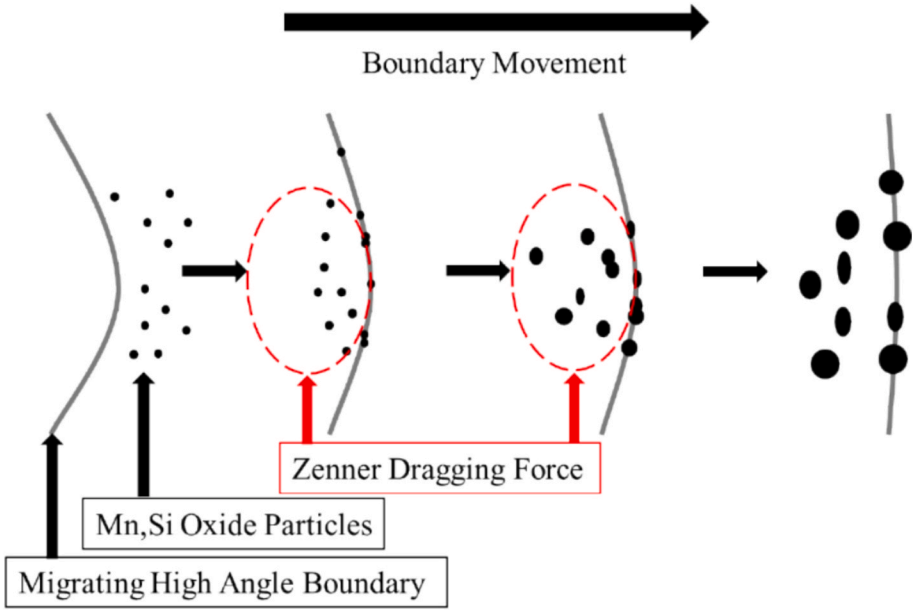

Fig. 24. Schematic showing the interaction between coarsening of oxide particles with a migrating high-angle boundary during strain induced boundary migration mechanism. []
Adapted from 30.

When the annealing temperature is increased to 1200 °C (HT3), the oxide pinning effects are significantly reduced due to the enhanced driving force generated at higher temperatures. Elevated temperatures promote greater atomic mobility, accelerating grain boundary migration and reducing the effectiveness of Zener pinning by oxide particles, which is why much greater recrystallisation percentages are achieved. The higher thermal energy facilitates the dissolution and coarsening of oxides, weakening their ability to restrict boundary movement. Additionally, the increased driving force overcomes the resistance imposed by pinning particles, allowing more rapid grain growth and leading to microstructures clustered with more abnormally grown grains. As a result, the restrictive influence of oxide pinning diminishes considerably at 1200 °C, enabling more extensive recrystallisation and grain boundary migration.

Assuming an equal initial dislocation density of $1.30 \times 10^{14}/m^2$ for samples subjected to heat treatments at 1150 °C and 1200 °C, the differences in recrystallisation behaviour can be attributed primarily to the interplay between driving pressure, pinning pressure, and grain boundary mobility during thermal exposure. Both samples begin with the same stored strain energy, representing the driving pressure for recrystallisation, and initially exhibit similar pinning pressures from dislocations and second-phase particles in the as-built microstructure.

During heat treatment, dislocation recovery and particle coarsening modify these factors differently at each temperature. The Zener pinning pressure was calculated to assess particle pinning evolution. At 1050 °C, the average particle radius increased from 0.0178 μm to 0.0747 μm while the fraction volume lowered to 0.41 % from 0.533 %, leading to a particle pinning pressure of 0.055 MPa, significantly lower than the driving pressure. At 1050 °C, recrystallisation does not occur primarily due to limited thermal activation that restricts grain boundary mobility. Although the driving pressure may exceed the pinning pressure, the temperature is insufficient to provide the necessary energy for grain boundaries to move and for recrystallised grains to nucleate and grow. This low grain boundary mobility slows down the recrystallisation kinetics significantly, preventing the process from progressing even when the thermodynamic conditions appear favourable. Additionally, complex particle distributions and recovery processes may further inhibit boundary migration and reduce the effective driving pressure, contributing to the suppression of recrystallisation at this temperature. While at higher temperatures of 1150 °C resulted in a reduction of pinning pressure to approximately 3.75 % of the as-built value, at 1200 °C, the particle radius further increases to 0.4392 μm with a volume fraction of 0.842 %, yielding a pinning pressure about 6.4 % of the initial as-built state. Despite this slightly higher pinning pressure at 1200 °C, the overall resistance to grain boundary movement remains significantly reduced compared to as-built conditions.

At 1150 °C, moderate dislocation recovery reduces the driving pressure somewhat, but grain boundary mobility is limited by lower atomic diffusion rates. This combination of oxide induced pinning pressure and lower driving pressure due to recovery restricts recrystallisation progression, leading to approximately 72 % recrystallisation in the 0.6 mm HT2 sample. At 1200 °C, more extensive recovery further decreases the driving pressure, but a higher grain boundary mobility rate enables faster grain boundary migration. This enhanced mobility overcomes the marginal pinning pressure exerted by the coarser oxides within, resulting in nearly complete recrystallisation (~99 %).

In summary, although both driving pressure and pinning pressure decrease during heat treatment, the dominant factor controlling recrystallisation extent is the grain boundary mobility combined with the oxide distribution, which increases markedly with temperature. This allows recrystallisation to proceed more fully at 1200 °C, highlighting the critical role of temperature-dependent kinetics in microstructural evolution.

Furthermore, at 1200 °C, the thermal energy is significantly greater, increasing atomic diffusivity and lowering the critical driving force required for boundary migration. This temperature-dependent increase in grain boundary mobility enables boundaries to overcome local pinning sites more readily, promoting more recrystallisation and grain growth. The presence of a small number of grains significantly larger than the matrix indicates the onset of abnormal grain growth (AGG) as classically defined by a bimodal grain size distribution [19] produced from the stop and go recrystallisation mechanism. While there is no universally accepted area-based threshold for identifying abnormal grains in experimental literature, phase-field simulations [48] suggest that grains with equivalent diameters exceeding 3.5x the mean diameter corresponding to areas approximately 12x larger than the mean, this behaviour is consistent with AGG which can be expressed as follows:

$$D_{Abnorm=}\frac{D_{Max}}{D_{avg}} > 3.5 \tag{3}$$

Where, if the grain diameter is more than 3.5x the average grain diameter it can be considered as abnormal, marking the onset or presence of abnormal grain growth. Therefore this criterion was applied to the samples within this study.

Table 8 demonstrates that a significant number of grains exceed the defined size threshold, corroborating the occurrence of AGG under the applied heat treatment regimes, with a more pronounced effect observed in HT2 compared to HT3. The reduced average grain size in HT2, attributable to its partial recrystallisation, effectively impedes grain coarsening and preserves a finer microstructural scale. In contrast, the fully recrystallised HT3 condition facilitates more uniform grain growth, yielding larger average grain sizes yet a diminished relative fraction of abnormally grown grains. This indicates that complete homogenisation promotes a microstructure characterised by a greater prevalence of uniformly large grains, thereby suppressing the nucleation and growth of abnormal grains. Given that each microstructural condition exhibits distinct average grain diameters, the ratio of maximum grain diameter (D_{Max}) to average grain diameter (D_{avg}) varies accordingly. Nonetheless, the dataset consistently reveals that HT2 samples possess a higher proportion of abnormally large grains relative to HT3. Through previous research, AGG in SS316L is generally reported to initiate within the temperature range of 1000–1200 °C [50]. In this regime, certain grain boundaries exhibit a localised velocity advantage, promoting preferential and accelerated grain growth compared to the surrounding matrix. This localised enhancement in grain boundary mobility leads to the

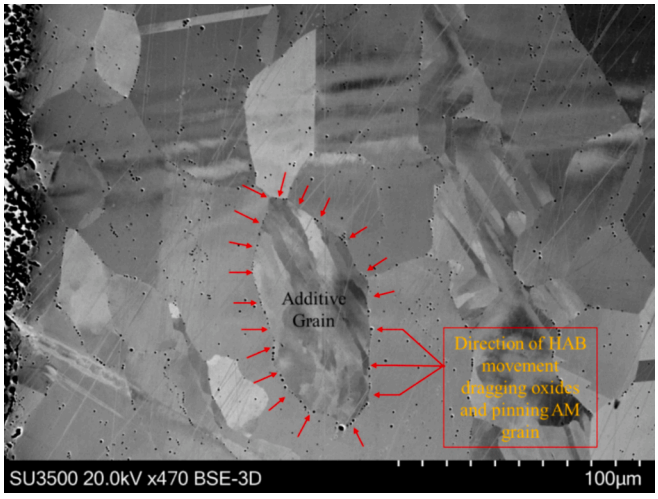

Fig. 25. Annotated backscattered image of LB-PBF SS316L thin-walled 0.6 mm sample subjected to HT2 conditions (1150 °C, 135 min) – XZ microstructural plane. Image illustrates the abnormally-grown recrystallised grains that have grown and dragged oxides to the boundary of a non-recrystallised AM grain. The boundary migration has ceased due to insufficient driving force, therefore leaving oxides precipitated at the grain boundaries.

Table 8
Abnormal grain count for HT2 and HT3 conditions.

HT ID	Thickness (mm)	Avg. Grain Diameter (μm)	Total grain count	Abnormal grain count
2	0.3	19.73	99	1
	0.4	27.85	142	2
	0.5	25.77	280	6
	0.6	24.39	375	12
	0.8	25.56	610	8
	1	26.14	796	13
	1.8	23.98	1309	33
3	0.8	28.99	300	5
	1	31.40	413	5
	1.8	32.02	811	9

development of abnormally large grains, consistent with the typical AGG behaviour observed [48]. So in the case of this study, the HT3 (1200 °C) conditions are on the tail end of the temperature range and therefore the abnormal grain ratio drops off, compared to temperature of 1150 °C.

5. Conclusions

In this study, a series of LB-PBF SS316L thin-walled samples were manufactured and subjected to one of three heat treatment annealing processes at temperatures ranging from 1050 °C to 1200 °C and compared to the as-built equivalent. The aim of the research was to assess the effect of sample thickness on the microstructural morphology, and most importantly, recrystallisation behaviour of thin-walled samples. The main conclusions are as follows:

1. In the as-built condition, the microstructure of LB-PBF SS316L changes with an increasing wall thickness. In thinner samples (0.2–0.4 mm), grains preferentially grew in the <001> crystallographic orientation, and displayed a morphology that would orient towards the centre of the wall due to the thermal gradient attributed to the LB-PBF process. Once the wall thickness exceeds 0.4 mm, the <101> orientation was dominant.
2. A temperature of 1050 °C was proven to have no significant effect on the microstructure with little to no recrystallisation observed, as the samples resembled morphologies similar to the as-built state. However, this temperature slightly altered the crystallographic texture, particularly in the thinner samples. Also, grain size increased by a factor of 2.
3. At 1150 °C, partial recrystallisation was observed, with a small fraction of long-columnar grains being replaced by an uneven distribution of equiaxed, normally grown, and abnormally large "homogenised" grains. The sluggish recrystallisation at this temperature was primarily attributed to oxide pinning, which restricted grain boundary mobility and impeded the formation of a fully recrystallised microstructure. Analysis of GND density, as well as HAB and LAB frequencies, did not reveal any clear correlation with the final recrystallisation percentages, suggesting that oxide pinning played a more dominant role in controlling the recrystallisation process.
4. At 1200 °C (HT3), near 100 % recrystallisation was consistently achieved across all sample thicknesses (0.8 mm, 1 mm and 1.8 mm), indicating that the elevated temperature was sufficient to overcome the strong oxide particle pinning that had previously hindered recrystallisation at lower temperatures. This temperature also led to a significant increase in grain growth, with an expansion factor of 1 to 1.5 observed in all samples. Despite the enhanced recrystallisation and grain growth, the frequency of annealing twins remained consistent between 1150 °C (HT2) and 1200 °C (HT3), suggesting that twin formation was not significantly influenced by the temperature increase in this range.
5. From EBSD analysis on each of the samples with varying wall thicknesses and subjected to one of the three post process heat treatment conditions, no single microstructural parameter was found to prominently control the hardness response of the material. This included grain size, aspect ratio, frequency of LABs, percentage of twin boundaries, texture, recrystallisation percentage, in addition to the thickness of each respective wall. Therefore, it is suggested that future studies should focus on alternative property characterisation methods to understand whether a trend can be derived between the resulting microstructures and the mechanical performance.
6. Prior to this study, it was believed that the driving force for recrystallisation was primarily due to the presence of geometrically necessary dislocations (GNDs). However, the results of this study show that GNDs do not have a significant correlation with recrystallisation. Although high stored energy from GNDs was present, it did not lead to substantial recrystallisation, indicating that the primary mechanism in the thin-walled samples was strain-induced boundary migration (SIBM). Additionally, the presence of Mn-Si oxide particle pinning was found to significantly limit grain boundary movement, further hindering recrystallisation.

CRediT authorship contribution statement

Charlie Bevan: Writing – original draft, Validation, Investigation, Formal analysis. **Nicholas Barnard:** Writing – original draft, Investigation. **Thomas Jones:** Writing – original draft, Supervision, Methodology, Conceptualization. **Robert Lancaster:** Writing – original draft, Supervision, Project administration, Methodology, Funding acquisition, Conceptualization.

Declaration of competing interest

The authors declare that they have no known competing financial interests or personal relationships that could have appeared to influence the work reported in this paper.

Acknowledgements

The current research was solely funded by Rolls-Royce plc. The provision of a research bursary, materials, and supporting information from Rolls-Royce plc. is gratefully acknowledged.

Data availability

The data that has been used is confidential.

References

[1] F. Careri, R.H.U. Khan, C. Todd, M.M. Attallah, Additive manufacturing of heat exchangers in aerospace applications: a review, Appl. Therm. Eng. 235 (Nov. 2023) 121387, https://doi.org/10.1016/J.APPLTHERMALENG.2023.121387.
[2] W. Abd-Elaziem, S. Elkatatny, A.E. Abd-Elaziem, M. Khedr, M.A. Abd El-Baky, M. A. Hassan, M. Abu-Okail, M. Mohammed, A. Järvenpää, T. Allam, A. Hamada, On the current research progress of metallic materials fabricated by laser powder bed fusion process: a review, J. Mater. Res. Technol. 20 (Sep. 2022) 681–707, https://doi.org/10.1016/J.JMRT.2022.07.085.
[3] P.A. Hooper, Melt pool temperature and cooling rates in laser powder bed fusion, Addit. Manuf. 22 (Aug. 2018) 548–559, https://doi.org/10.1016/j.addma.2018.05.032.
[4] A.J. Godfrey, J. Simpson, D. Leonard, K. Sisco, R.R. Dehoff, S.S. Babu, Heterogeneity and solidification pathways in additively manufactured 316L stainless steels, Metall. Mater. Trans. A Phys. Metall. Mater. Sci. 53 (9) (Sep. 2022) 3321–3340, https://doi.org/10.1007/s11661-022-06747-6.
[5] Z.E. Tan, J.H.L. Pang, J. Kaminski, H. Pepin, Characterisation of porosity, density, and microstructure of directed energy deposited stainless steel AISI 316L, Addit. Manuf. 25 (Jan. 2019) 286–296, https://doi.org/10.1016/j.addma.2018.11.014.
[6] F. Khodabakhshi, M.H. Farshidianfar, A.P. Gerlich, M. Nosko, V. Trembošová, A. Khajepour, Microstructure, strain-rate sensitivity, work hardening, and fracture behavior of laser additive manufactured austenitic and martensitic stainless steel

structures, Mater. Sci. Eng. A 756 (May 2019) 545–561, https://doi.org/10.1016/J.MSEA.2019.04.065.
[7] R.I. Revilla, G. Li, R. Pion, K. Marcoen, F. Andreatta, L. Fedrizzi, K. Vanmeensel, I. De Graeve, Effect of heat treatment on the microstructure and pitting corrosion behavior of 316L stainless steel fabricated by different additive manufacturing methods (L-PBF versus L-DED): comparative investigation exploring the role of microstructural features on passivity, Corros. Sci. 228 (Mar. 2024) 111814, https://doi.org/10.1016/J.CORSCI.2023.111814.
[8] A. Fedorenko, B. Fedulov, Y. Kuzminova, S. Evlashin, O. Staroverov, M. Tretyakov, E. Lomakin, I. Akhatov, Anisotropy of mechanical properties and residual stress in additively manufactured 316l specimens, Materials 14 (23) (2021) Dec, https://doi.org/10.3390/ma14237176.
[9] M.J. Heiden, L.A. Deibler, J.M. Rodelas, J.R. Koepke, D.J. Tung, D.J. Saiz, B. H. Jared, Evolution of 316L stainless steel feedstock due to laser powder bed fusion process, Addit. Manuf. 25 (Jan. 2019) 84–103, https://doi.org/10.1016/J.ADDMA.2018.10.019.
[10] T. DebRoy, H.L. Wei, J.S. Zuback, T. Mukherjee, J.W. Elmer, J.O. Milewski, A. M. Beese, A. Wilson-Heid, A. De, W. Zhang, Additive manufacturing of metallic components – Process, structure and properties, Prog. Mater Sci. 92 (Mar. 2018) 112–224, https://doi.org/10.1016/J.PMATSCI.2017.10.001.
[11] C. Yu, Y. Zhong, P. Zhang, Z. Zhang, C. Zhao, Z. Zhang, Z. Shen, W. Liu, Effect of build direction on fatigue performance of L-PBF 316L stainless steel, Acta Metall. Sin. (Engl. Lett.) 33 (4) (Apr. 2020) 539–550, https://doi.org/10.1007/s40195-019-00983-3.
[12] X. Tong, C. Lu, Z. Huang, C. Zhang, F. Chen, Microstructures and mechanical properties of crack-free 316L stainless steel and Inconel 625 joint by using Laser Engineered Net Shaping, Opt. Laser Technol. 155 (Nov. 2022), https://doi.org/10.1016/j.optlastec.2022.108357.
[13] L. Cui, S. Jiang, J. Xu, R.L. Peng, R.T. Mousavian, J. Moverare, Revealing relationships between microstructure and hardening nature of additively manufactured 316L stainless steel, Mater. Des. 198 (Jan. 2021) 109385, https://doi.org/10.1016/J.MATDES.2020.109385.
[14] S. Ren-ho, X. Jian-ying, H. Dong-po, Characteristics of Mechanical Properties and Microstructure for 316L Austenitic Stainless Steel, 2011. [Online]. Available: www.sciencedirect.com.
[15] R. Casati, J. Lemke, M. Vedani, Microstructure and fracture behavior of 316L austenitic stainless steel produced by selective laser melting, J. Mater. Sci. Technol. 32 (8) (Aug. 2016) 738–744, https://doi.org/10.1016/J.JMST.2016.06.016.
[16] D. Kong, X. Ni, C. Dong, L. Zhang, C. Man, X. Cheng, X. Li, Anisotropy in the microstructure and mechanical property for the bulk and porous 316L stainless steel fabricated via selective laser melting, Mater. Lett. 235 (Jan. 2019) 1–5, https://doi.org/10.1016/J.MATLET.2018.09.152.
[17] R. Wrobel, L. Del Guidice, P. Scheel, N. Abando, X. Maeder, M. Vassiliou, E. Hosseini, R. Spolenak, C. Leinenbach, Influence of wall thickness on microstructure and mechanical properties of thin-walled 316L stainless steel produced by laser powder bed fusion, Mater. Des. 238 (Feb. 2024) 112652, https://doi.org/10.1016/J.MATDES.2024.112652.
[18] D.N. Croft, Types of heat treatment, Heat Treatment of Welded Steel Structures, pp. 9–20, Jan. 1996, doi: 10.1533/9781845698812.9.
[19] F.J. Humphreys, M. Hatherly, Recrystallization and related annealing phenome, Pergamon Press, Oxford, 1995.
[20] M. Laleh, E. Sadeghi, R.I. Revilla, Q. Chao, N. Haghdadi, A.E. Hughes, W. Xu, I. De Graeve, M. Qian, I. Gibson, M.Y. Tan, Heat treatment for metal additive manufacturing, Prog. Mater Sci. 133 (Mar. 2023) 101051, https://doi.org/10.1016/J.PMATSCI.2022.101051.
[21] N. Chen, G. Ma, W. Zhu, A. Godfrey, Z. Shen, G. Wu, X. Huang, Enhancement of an additive-manufactured austenitic stainless steel by post-manufacture heat-treatment, Mater. Sci. Eng. A 759 (Jun. 2019) 65–69, https://doi.org/10.1016/J.MSEA.2019.04.111.
[22] Bertsch, K.M.; Meric de Bellefon, G.; Kuehl, B.; and Thoma, D.J., 'Origin of dislocation structures in an additively manufactured austenitic stainless steel 316L', *Acta Mater*, vol. 199, pp. 19–33, Oct. 2020, doi: 10.1016/J.ACTAMAT.2020.07.063.
[23] P. Deng, M. Song, J. Yang, Q. Pan, S. McAllister, L. Li, B.C. Prorok, X. Lou, On the thermal coarsening and transformation of nanoscale oxide inclusions in 316L stainless steel manufactured by laser powder bed fusion and its influence on impact toughness, Mater. Sci. Eng. A 835 (Feb. 2022) 142690, https://doi.org/10.1016/J.MSEA.2022.142690.
[24] X. Lou, P.L. Andresen, R.B. Rebak, Oxide inclusions in laser additive manufactured stainless steel and their effects on impact toughness and stress corrosion cracking behavior, J. Nucl. Mater. 499 (Feb. 2018) 182–190, https://doi.org/10.1016/J.JNUCMAT.2017.11.036.
[25] M.F. Ashby, R.M.A. Gentamore, The dragging of small oxide particles by migrating grain boundaries in copper, Acta Metall. 16 (9) (Sep. 1968) 1081–1092, https://doi.org/10.1016/0001-6160(68)90043-6.
[26] S. Gao, Z. Hu, M. Duchamp, P.S.S.R. Krishnan, S. Tekumalla, X. Song, M. Seita, Recrystallization-based grain boundary engineering of 316L stainless steel produced via selective laser melting, Acta Mater. 200 (Nov. 2020) 366–377, https://doi.org/10.1016/J.ACTAMAT.2020.09.015.
[27] E. de Sonis, S. Dépinoy, P.F. Giroux, H. Maskrot, L. Lemarquis, O. Hercher, F. Villaret, A.F. Gourgues-Lorenzon, Dependency of recrystallization kinetics on the solidification microstructure of 316L stainless steel processed by laser powder bed fusion (LPBF), Mater. Charact. 194 (Dec. 2022) 112370, https://doi.org/10.1016/J.MATCHAR.2022.112370.
[28] L.S. Aota, P. Bajaj, K.D. Zilnyk, E.A. Jägle, D. Ponge, H.R.Z. Sandim, D. Raabe, Recrystallization kinetics, mechanisms, and topology in alloys processed by laser powder-bed fusion: AISI 316L stainless steel as example, Materialia (Oxf) 20 (Dec. 2021), https://doi.org/10.1016/j.mtla.2021.101236.
[29] T. Voisin, J.B. Forien, A. Perron, S. Aubry, N. Bertin, A. Samanta, A. Baker, Y. M. Wang, New insights on cellular structures strengthening mechanisms and thermal stability of an austenitic stainless steel fabricated by laser powder-bed-fusion, Acta Mater. 203 (Jan. 2021) 116476, https://doi.org/10.1016/J.ACTAMAT.2020.11.018.
[30] Deng, P. The origins of nanoscale oxide inclusion and its evolution in additively manufactured austenitic stainless steel during laser powder bed fusion and post heat treatment, Dissertation, Auburn University, 2020.
[31] W. Beard, R. Lancaster, N. Barnard, T. Jones, J. Adams, The influence of surface finish and build orientation on the low cycle fatigue behaviour of laser powder bed fused stainless steel 316L, Mater. Sci. Eng. A 864 (Feb. 2023) 144593, https://doi.org/10.1016/j.msea.2023.144593.
[32] R. Douglas, W. Beard, N. Barnard, S. Lee, S. Shao, N. Shamsaei, T. Jones, R. Lancaster, The influence of energy density on the low cycle fatigue behaviour of laser powder bed fused stainless steel 316L, Int. J. Fatigue 181 (Apr. 2024) 108123, https://doi.org/10.1016/j.ijfatigue.2023.108123.
[33] A. Ayad, N. Allain-Bonasso, N. Rouag, F. Wagner, Grain orientation spread values in if steels after plastic deformation and recrystallization, Mater. Sci. Forum Trans. Tech. Publications Ltd (2012) 269–272, https://doi.org/10.4028/www.scientific.net/MSF.702-703.269.
[34] Pinto, F.C.; Aota, L.S.; Souza Filho, I.R.; Raabe, D.; and Sandim, H.R.Z.; , 'Recrystallization in non-conventional microstructures of 316L stainless steel produced via laser powder-bed fusion: effect of particle coarsening kinetics', *J Mater Sci*, vol. 57, no. 21, pp. 9576–9598, Jun. 2022, doi: 10.1007/s10853-021-06859-1.
[35] W. Liu, C. Liu, Y. Wang, H. Zhang, H. Ni, Effect of heat treatment on the corrosion resistance of 316L stainless steel manufactured by laser powder bed fusion, J. Mater. Res. Technol. (Aug. 2024), https://doi.org/10.1016/J.JMRT.2024.08.194.
[36] Petroušek, P.; Kvačkaj, T.; Bidulská, J.; Bidulský, R.; Grande, M.A.; Manfredi, D.; Weiss, K.P.; Kočiško, R.; Lupták, M.; and Pokorný, I.; Investigation of the Properties of 316L Stainless Steel after AM and Heat Treatment', Materials, vol. 16, no. 11, Jun. 2023, doi: 10.3390/ma16113935.
[37] D. Riabov, A. Leicht, J. Ahlström, E. Hryha, Investigation of the strengthening mechanism in 316L stainless steel produced with laser powder bed fusion, Mater. Sci. Eng. A 822 (Aug. 2021) 141699, https://doi.org/10.1016/J.MSEA.2021.141699.
[38] P.A. Manohar, F. Chandra, Five decades of the Zener Equation, ISIJ Int. 38 (9) (1998) 913–924.
[39] R.A. Varin, Grain boundary diffusion and free energy during the recrystallization of type 316 stainless steel, Mater. Sci. Eng. 66 (1) (Sep. 1984) 97–105, https://doi.org/10.1016/0025-5416(84)90144-7.
[40] H. Buken, E. Kozeschnik, A model for static recrystallization with simultaneous precipitation and solute drag, Metall. Mater. Trans. A Phys. Metall. Mater. Sci. 48 (6) (Jun. 2017) 2812–2818, https://doi.org/10.1007/s11661-016-3524-5.
[41] E. Garlea, H. Choo, C.C. Sluss, M.R. Koehler, R.L. Bridges, X. Xiao, Y. Ren, B. H. Jared, Variation of elastic mechanical properties with texture, porosity, and defect characteristics in laser powder bed fusion 316L stainless steel, Mater. Sci. Eng. A 763 (Aug. 2019) 138032, https://doi.org/10.1016/J.MSEA.2019.138032.
[42] R.W. Fonda, D.J. Rowenhorst, C.R. Feng, A.J. Levinson, K.E. Knipling, S. Olig, A. Ntiros, B. Stiles, R. Rayne, The effects of post-processing in additively manufactured 316L stainless steels, Metall. Mater. Trans. A Phys. Metall. Mater. Sci. 51 (12) (Dec. 2020) 6560–6573, https://doi.org/10.1007/s11661-020-06039-x.
[43] Bertsch, K.M.; Meric de Bellefon, G.; Kuehl, B.; and Thoma, D.J.; , 'Origin of dislocation structures in an additively manufactured austenitic stainless steel 316L', Acta Mater, vol. 199, pp. 19–33, Oct. 2020, doi: 10.1016/J.ACTAMAT.2020.07.063.
[44] D.N. Lee, The evolution of recrystallization textures from deformation textures, Scr. Metall. Mater. 32 (10) (May 1995) 1689–1694, https://doi.org/10.1016/0956-716X(95)00256-U.
[45] T. Philippe, P.W. Voorhees, Ostwald ripening in multicomponent alloys, Acta Mater. 61 (11) (Jun. 2013) 4237–4244, https://doi.org/10.1016/J.ACTAMAT.2013.03.049.
[46] S. Chen, G. Ma, G. Wu, A. Godfrey, T. Huang, X. Huang, Strengthening mechanisms in selective laser melted 316L stainless steel, Mater. Sci. Eng. A 832 (Jan. 2022) 142434, https://doi.org/10.1016/J.MSEA.2021.142434.
[47] Aota, L.S.; Bajaj, P.; Zilnyk, K.D.; Ponge, D.; and Sandim, H.R.Z.; , 'The origin of abnormal grain growth upon thermomechanical processing of laser powder-bed fusion alloys', Materialia (Oxf), vol. 20, p. 101243, Dec. 2021, doi: 10.1016/J.MTLA.2021.101243.
[48] Liu, Y.; Militzer, M.; and Perez, M.; 'Phase field modelling of abnormal grain growth', Materials, vol. 12, no. 24, Dec. 2019, doi: 10.3390/MA12244048.
[49] K.H. Blixt, H. Hallberg, Grain boundary and particle interaction: Enveloping and pass-through mechanisms studied by 3D phase field crystal simulations, Mater. Des. 220 (Aug. 2022) 110845, https://doi.org/10.1016/J.MATDES.2022.110845.
[50] L. Mizera, J.W. Wyrzykowski, K.J. Kurzydlowski, Description of the kinetics of normal and abnormal grain growth in austenitic stainless steel, Mater. Sci. Eng. A 104 (1988) 157–162.